universität wien

MASTERARBEIT / MASTER'S THESIS

Titel der Masterarbeit / Title of the Master's Thesis

„Microstructure, shape and crystallographic orientation relationships of inclusions in metapelite garnet (Xanthi, Greece)“

verfasst von / submitted by

Mike Maurice Müller, B.Sc.

angestrebter akademischer Grad / in partial fulfilment of the requirements for the degree of

Master of Science (MSc)

Wien, 2023 / Vienna, 2023

Studienkennzahl lt. Studienblatt / degree programme code as it appears on the student record sheet:	UA 066 815
Studienrichtung lt. Studienblatt / degree programme as it appears on the student record sheet:	Masterstudium Erdwissenschaften UG2002
Betreut von / Supervisor:	Univ.-Prof. Dr. Rainer Abart
Mitbetreut von / Co-Supervisor:	Mag. Dr. Gerlinde Habler

Acknowledgements

I humbly attribute the attainment of my master's degree - as evidenced by this written thesis - to the invaluable contributions of the brilliant team that surrounded me during my journey. Their constant feedback proved to be a cornerstone of my progress.

Above all, my deepest gratitude goes to Gerlinde Habler, whose co-supervision opened the doors to this fascinating topic and who accompanied me through countless hours of measurements, providing insightful answers to my questions.
I also extend my thanks to Vicky Kohn for her willingness to engage in fruitful discussions that always led to the discovery of sound solutions.
Also, the support of Taisia Alifirova has been an steady source of encouragement.

To Rainer Abart, I am indebted for his commendable commitment to the solid interpretation and dependable supervision of my work.
I also extend my gratitude to Tom Griffiths for his lively discussions and for providing the essential mTex script, as well as for patiently guiding me in its use.
I must express my sincere appreciation to all the individuals who fostered a collegial environment that made each day enjoyable and motivating.
In particular, Ilka Wünsche deserves special mention for allowing me to participate in the sample preparation with curiosity, and for ensuring proper sample preparation that delighted me to no end.
Andreas Wagner's contribution to the sample preparation is also deeply appreciated.
I am also grateful to Sebastian Stumpf for the opportunity to work with the micro-CT method, which quickly captured my enthusiasm.

Lastly, I cannot overstate my appreciation to my family and partner, whose heartwarming support and encouragement made this accomplishment possible. My gratitude also extends to my friends, whose unwavering interest in my success was an ever-present source of inspiration.

Abstract

Metapelitic garnet-kyanite gneiss from the Kimi Complex (Rhodope Metamorphic Complex), north of the city Xanthi, Greece, was subject to a detailed investigation to assess its mineral content and the inclusion microstructure and texture in garnet. A suite of advanced analytical techniques was employed, including optical microscopy, micro computed tomography, SEM imaging methods, SEM-EDX, SEM-EBSD, and Raman spectroscopy. Results of thermobarometry based on Raman spectroscopy are in line with peak metamorphic conditions reported in the literature.
A further analysis of the inclusion microstructure in garnet allowed to distinguish several different growth zones in garnet and characteristic domains within these zones. The micro-inclusions in two different garnet domains were the focus of comprehensive microstructure and texture analysis. Based on the inclusion microstructure, the first garnet domain was defined by the presence of abundant sub-micron sized rutile inclusions that are arranged as (curvi)linear inclusion trails oriented parallel to the local growth direction of the host garnet crystal, referred to as "trail domain." The second garnet domain was defined by abundant rutile needles with strict shape preferred orientation (SPO), referred to as the "needle domain". These rutile needles with SPO but different aspect ratios were observed within the entirety of the studied garnets.
Electron backscatter diffraction (EBSD) analysis was performed to investigate crystallographic orientation relationships (COR) between the inclusion and host phases. Combination of the microstructural and crystallographic data showed a shape orientation relationship (SOR) between rutile needles and the garnet host in the needle domain. There, the elongation of the rutile needles aligns with $< 111 >_{Grt}$ directions. Further, the elongation of the rutile needles occurs strictly along the $< 103 >_{Rt}$, which therefore, correlates with an axial relationship between rutile needle and garnet host lattice.
Results from the statistical analysis of the distribution of rutile needles with particular SPO indicate that, in the trail domain, those rutile needles with an SPO at high angle with respect to the growth facet plane of the particular garnet sector predominate over SPO directions lying parallel to this garnet plane. Contrastingly, the distribution of rutile needles with strict SPO was observed to be evenly balanced between the different crystallographic equivalent $< 111 >_{Grt}$ directions in the needle domain.

These findings suggest that the inclusion trails in the trail domain were formed through an attachment and overgrowth mechanism, syngenetic to garnet growth, while the needles with distinct SPO in the needle domain were likely a product of precipitation within a preexisting garnet lattice.
The correlation of microstructural properties of rutile inclusions with their crystallographic orientation relationship regarding the host crystal, yielded a strong link to the microstructural peculiarities of the studied inclusions. Comparison with other large EBSD data sets indicates that rutile inclusions in metapelite garnets follow similar trends of axial relationships, but show significant deviations, especially regarding specific CORs, and when considering different microstructural characteristics.
Still, when applying a consistent COR classification, large EBSD data sets correlated with microstructural observations, show potential for fingerprinting based on rutile inclusion - garnet host systems.

Kurzfassung

Metapelitischer Granat-Kyanit-Gneiss (Lokalität nördlich der Stadt Xanthi, Griechenland) aus dem Kimi Komplex, Rhodopen, wurde untersucht, um den Mineralgehalt und die Einschlussgefüge und -muster in Granat zu bestimmen. Dazu wurden optische Mikroskopie, Mikro-Computer-tomografie, SEM-Bildgebungsverfahren, SEM-EDX, SEM-EBSD und Raman-Spektroskopie verwendet. Die Ergebnisse der Thermobarometrie auf Grundlage der Raman-Spektroskopie zeigen, dass die metamorphischen Höchstbedingungen mit den Einschätzungen der Literatur übereinstimmen.
Detaillierte Analysen des Einschlussgefüges hat mehrere Granat Wachstumszonen und charakteristische Domänen innerhalb dieser Zonen offenbart. Die Mikro-Einschlüsse zweier Granat Domänen wurden daraufhingend detailliert auf ihre Mikrostruktur und Textur untersucht. Die erste Domäne wurde durch zahlreiche sub-mikrometer große Rutil Einschlüsse definiert, welche sich entlang von (kurvi)linearen Einschluss Spuren anordnen. Diese Spuren sind parallel entlang der lokalen Wachstumsrichtung von Granat Sektoren angeordnet. Diese mikrostrukturelle Granat Domäne wurde daher als "Trail-Domäne" bezeichnet. Die zweite Domäne wurde durch eine Vielzahl von Rutilnadeln mit strikten Form vorzugs-Orientierungen (SPO) definiert und als "Nadel-Domäne" bezeichnet. Diese Rutilnadeln wurden mit unterschiedlich ausgeprägten Streckungsverhältnissen im gesamten Granat beobachtet.
Die Elektronen-Rückgestreu-Diffraktions Analyse (EBSD) dient zur Untersuchung kristallografischer Orientierungsbeziehungen (COR) zwischen Einschluss- und Wirt-Kristall. Die Kombination mikrostruktureller mit kristallografischen Eigenschaften impliziert eine Form Orientierung (SOR) der Rutilnadeln im Granat Wirtskristall, welche die Längsrichtungen der Rutilnadeln intern entlang der $< 103 >_{Rt}$ und extern der $< 111 >_{Grt}$ beschreibt.
Ergebnisse der statistsichen Häufigkeits-Analyse der Verteilung von Rutil Einschlüssen mit strenger SPO deutet darauf hin, dass die Einschluss Spuren in der Trail-Domäne Rutil Einschlüsse mit SPOs bevorzug werden, deren Längsachsen einen grossen Winkel zu der jeweiligen Fläche der Wachstumsfacette des Granat Sektors eingehen, entgegen Einschlüssen mit SPO, deren Längsachsen parallel zu besagter Fläche des Granats liegen. Die Verteilung in der Nadel-Domäne wurden hingegen als gleichmäßig ausgewogen zwischen den kristallografisch equivalenten SPO $< 111 >_{Grt}$ Richtungen beobachtet. Diese Befunde legen nahe, dass die Einschlüsse in der Trail-Domäne durch einen Anhaftungs- und Überwachsungsmechanismus gebildet wurden, zeitgleich des Granat Wachstums. Die Rutilnadeln mit deutlicher SPO in der Nadel-Domäne hingegen sind ein Produkt von Fällungsreaktionen, welche nach dem Granat Wachstum, sprich in einem pre-existierenden Granat Kristallgitter, stattgefunden haben müssen.

Die Unterschiede in den Entstehungsszenarien werden ebenfalls in der COR-Klassifikation widergespiegelt. Die Ergebnisse des Ansatzes große Datensätze von Kristallorientierungen methodisch zu vergleichen, werden stark von den untersuchten Einschlüssen und ihren mikrostrukturellen Eigenheiten beeinflusst. Im Vergleich mit anderen EBSD-Datensätzen wurde beobachtet, dass solange die gleiche Klassifizierungsroutine angewandt wird, Metapelite ähnlichen Trends axialer Orientierungsbeziehungen folgen, aber spezifische CORs und mikrostrukturelle Eigenschaften stark abweichen.
Durch diese Studie werden, in Anbetracht der COR Klassifikation und mikrostruktureller Eigenschaften, Beziehungen von Einschlüssen im Wirtskristall für "Fingerprinting" als möglich erachtet.

Contents

List of Figures

1. Introduction

1.1. Motivation

The presence of numerous rutile micro-inclusions in garnet host crystals are a common phenomenon observed in a wide variety of rock types. The complexity and variability of the microstructural and textural rutile inclusions - garnet host relationships have given rise to the idea of using their characteristics to infer petrogenetic information from them. With the recent possibility to create large crystal orientation data sets based on Electron Backscatter Diffraction (EBSD) analysis, the complex crystallographic relationships between the two phases now can be encompassed. Through the systematic categorisation of crystallographic orientation relationships (COR) in correlation with shape orientation relationships (SOR), the inclusion fabric is expected to provide information on aspects of the origin of rutile inclusions in garnet. A preliminary study on rutile inclusions in garnet from a metapelitic gneiss from the locality Xanthi, already had shown systematics in the orientation relationships between the crystallographic lattices of rutile inclusions and their corresponding garnet host and potential formation mechanisms were postulated. The current study aims to combine COR data with microstructural data of rutile inclusions, and to compare these characteristics observed with sets of microstructurally different inclusions, for different growth sectors and growth zones of garnet. The new data set will then be compared with the preliminary COR data, in order to evaluate existing hypotheses on the origin of the studied inclusions.
The study is linked to the FWF-ARRS International Joint-project "GInA - Mineral inclusions in garnet: nanostructure-texture-genesis" (FWF I4285-N37; ARRS N1-0115).

1.2. Geological Setting

1.2.1. Geology of the Rhodopes Massif

The tectonometamorphic units of the Rhodope Massif occupy a central position in the Alpine belt, between the south west-verging Hellenides and the north-verging Balkanides. The so-calling Rhodope Metamorphic Complex (RMC) mostly consists of medium to high-grade pre-Alpine and Alpine metamorphic rocks and granitoids and represents the exhumed metamorphic core of the Alpine orogen of the Hellenides (Bosse et al., 2009; Mposkos et al., 2010, 2012, & the references therein). The RMC constitutes the largest and highest grade metamorphic part of the Alpine chain in Greece (Liati and Gebauer, 1999).
During the first mid-Mesozoic stage (110-90 Ma) the rocks of RMC underwent high-pressure metamorphism (eclogitic/amphibolitic-facies). Apart from regional metamorph-

ism a system of syn-metamorphic thrusts with south vergence has been reported. The second, extensional, stage (50-30 Ma) is connected with tectonic erosion of the syn-metamorphic thrust complex and is the origin of a system of gently dipping detachment faults (Ivanov et al., 2000).
The distinct geological units of the RMC were metamorphosed to high pressures at different times, favoring the former existence of different terranes. The exhumation rates were relatively high (Liati and Gebauer, 1999). The earliest exhumed and structurally uppermost entity is the Kimi Complex, followed by the Sidironeron (Central Rhodope) and Kechros (East Rhodope) Complexes and then by the Pangaeon Complex which forms the Rhodope metamorphic core complex (Perraki et al., 2006).

1.2.2. Geology of sampling location Xanthi

The metapelitic gneiss of the sampling site north of Xanthi is located in the eastern part of the Rhodope Domain, the Alpine Rhodopes Suture Zone (RSZ) between upper and lower tectonic units. According to Krenn et al. (2010) this suture zone is also subdivided in a lower and an upper part. The lower part is made up of different types of rocks, such as paragneiss (this studie's sample material), orthogneiss, quartzitic gneiss, amphibolites, hornblende-plagioclase gneiss, and marbles with interspersed amphibolite lenses. There are also concordant pegmatoids, which can be up to a meter thick and sometimes contain kyanite and corundum. The upper part as well is comprised of orthogneisses and paragneisses that have been migmatized, as well as ultramafic rocks like serpentinites, spinel-garnet-peridotites, and garnet-pyroxenites. It also includes marbles, eclogites that have been retrogressed and have leucosomes that are usually found in quartzo-feldspathic gneisses, and a network of small, discordant pegmatoid veins. Due to intense folding, the rocks of the upper part can be found right next to the rocks of the lower part.
Focusing on the lower part of the RSZ three main ductile deformation stages are observed (Krenn et al., 2010). The first, D1 stage, is presented by L > S gneisses, which entail plagioclase and garnet porphyroclasts. Recrystallised quartz is observed within garnet in this lineation. An folding event of the second deformation stage (D2) produces recumbent isoclinal folds of D1-related constrictional gneisses around marbles (Krenn et al., 2010). The next deformation stage (D3) overprints the prior folds by a meter scale folding, which results in a fold interference pattern in the gneisses. The latter fold is also preserved in locally developed asymmetric pressure shadows around mineral porphyroclasts. In conclusion the metamorphic history of Greek Rhodpope started from Early to Middle Jurassic time due to continent–continent collision between the Lower and Upper Terrane (Krenn et al., 2008, 2010). The gneiss also underwent two stages of mid-Mesozoic deformation stages, the high grade D2 stage and the D3 stage of decreasing pressure and temperature metamorphism conditions.

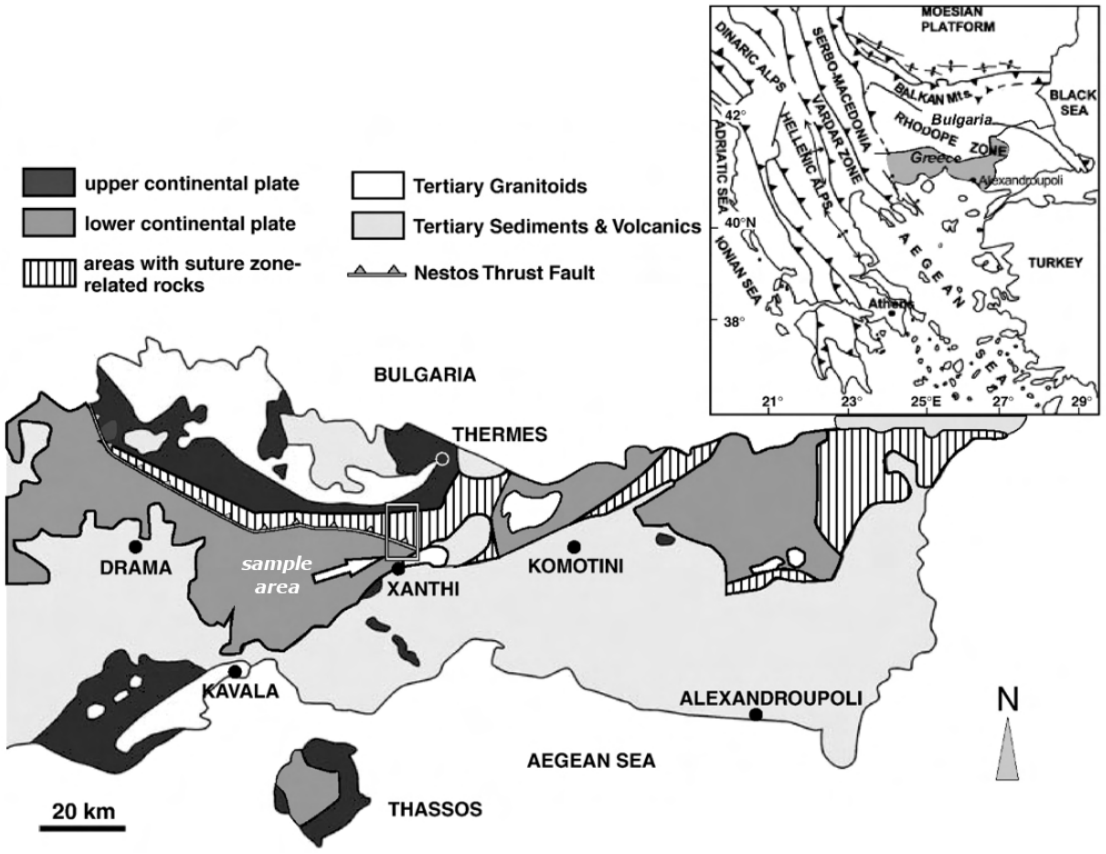

Figure 1.: Geological overview of the Greek Rhodope Metamorphic Complex (modified after Krenn et al. (2008, Fig. 1)). The sampling site of the studied specimen is indicated by a rectangle.

1.3. Sample material

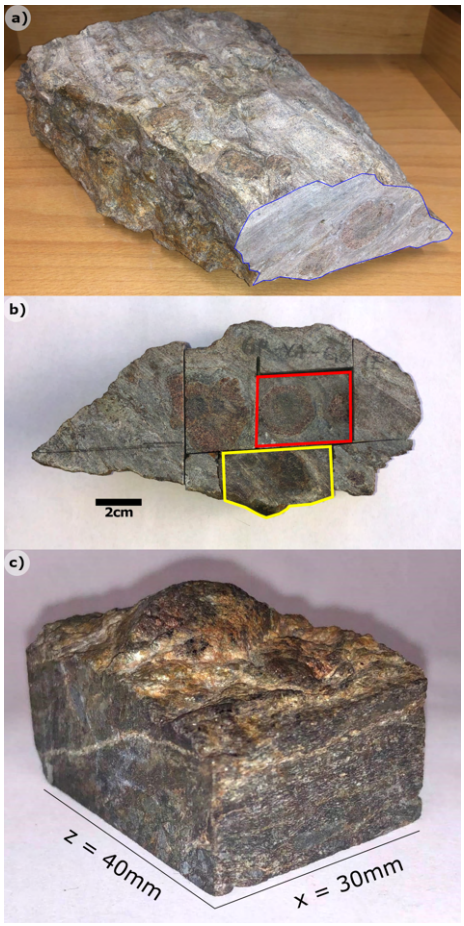

Figure 2.: (Caption next page.)

The rock sample XA-GO-1E analysed in this study is a Ky-Grt gneiss from the Xanthi area (indicated in Fig 1) in the Kimi Complex of the Greek Rhodope (Krenn et al., 2008, 2010; Proyer et al., 2013). The sampling site is an outcrop on the road Drama to Xanthi, where a brigde crosses Kosynthos river close to the junction to Echinos (coordinates: 41° 11.326, 24° 51.602).
The hand specimen is a metapelitic star-garnet, kyanite-bearing paragneiss with s and c' fabric. It contains centimetre sized subidiomorphic garnets embedded in rock matrix. This lithology and its assemblage (Grt, Ky ± Sil, Pl, Bt, white mica, Chl, Qz, with accessories like Ep/Zo, Tur, Rt, Ap and opaque phases) was investigated in earlier studies on fluid inclusions (Krenn et al., 2008) and TiO_2 precipitation in garnet (sample: *2R5*, Proyer et al., 2013).
Krenn et al. (2008) refined the P/T-path of rocks from the Xanthi area based on fluid inclusion data. Proyer et al. (2013) investigated garnet from metapelitic gneiss of the Xanthi area, reporting mineral compositional data from electron probe micro analysis (EPMA), as well as crystal orientation data from electron backscatter diffraction (EBSD) and transmission electron microscopy (TEM).
The peak P/T conditions of metamorphism that affected the rocks of this location are in discussion. While Mposkos and Krohe (2000) inferred ultra-high pressure (UHP) conditions ($P > 16kbar$) based on the presence of nanodiamonds, Krenn et al. (2008) estimated the peak P/T conditions for the stage of *"D2 shear deformation"* to $13kbar$ at $700°C$. Proyer et al. (2013) used thermobarometers that yielded two possible conditions of peak metamorphism, namely 850 ± 50 °C / $14.5 \pm 1.8kbar$ (Thermocalc), or $620 - 660°C$ / $11 - 16\,kbar$ (GASP/PET).
For the studied Ky-Grt gneiss sample seven thin sections were prepared: thin sections XA-GO-1E_A,_B,_C, _I existed prior to this study and are cut in an unknown direction. From the specimen in figure 2 a) the thin sections XA-GO-1E_II,_IIIa,_IIIb were newly prepared based on the methodology described in section 3.4 below.
XA-GO-1E_II was cut perpendicular to the intersection-lineation (see figure 2 b)). XA-GO-1E_IIIa/b were cut perpendicular to a $\{110\}_{Grt}$ facet from the bulk in figure 2 c) after micro-CT analysis of the 3D geometry of a selected garnet crystal.

Figure 2.: (Previous page.) a) Xanthi rock sample of kyanite and garnet-bearing gneiss with s and c' fabric, from which a hand piece was cut perpendicular to the intersection-lineation (blue trace).
b) Slice of the hand specimen after cutting, from which three thin sections were prepared. The red trace shows the location of thin section XA-GO-1E_II, which is perpendicular to the intersection-lineation, and the yellow trace marks the bulk for micro-CT analysis.
c) shows the dimensions of the rock chip marked by the yellow box in b), which was used for micro-CT analysis and for preparation of the thin sections XA-GO-1E_IIIa/b.

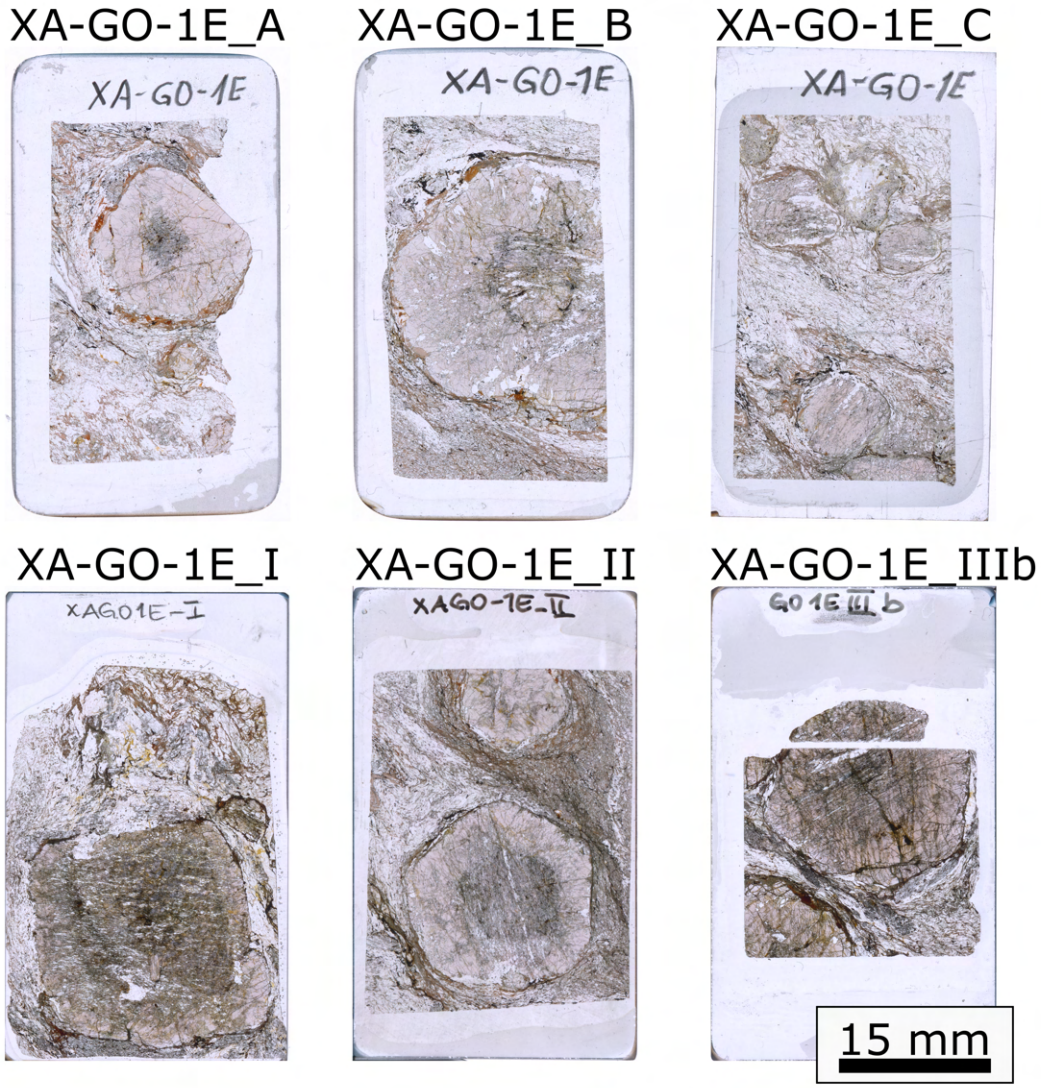

Figure 3.: All thin section of the Xanthi XA-GO-1E series (except for XA-GO-1E_IIIa, which is a mirrored version of XA-GO-1E_IIIb).
For more information see appendix A.1.

2. State of research

2.1. Sector zoning

Sector-zoning can occur in a variety of minerals. In sector zoned minerals the crystals are divided in several growth pyramids, the bases of which correspond to the crystal faces. In theory all growth pyramids are supposed to meet in the centre of the crystal and all crystallographically equivalent crystal faces have the same shape and interfacial energy (Rice et al., 2006). Sector zoning occurs as three different (but somewhat related) types: twin, chemical and textural sector-zoning (Rice and Mitchell, 1991).
Chemical sector-zoning is defined by different chemical compositions of crystallographically non-equivalent sectors, e.g.: often observed in pyroxenes. In garnet chemical sector-zoning was verified by EPMA ((Lessing and Standish, 1973), although there was no optical evidence by OM.
Twin sector zoning was discussed by Brown and Mason (1994) to cause birefringence in otherwise isotropic and isometric garnet. They observed sectored extinction in almandine garnet, as well as loss of symmetry determined by X-Ray Diffraction. Chemical and twin sector-zoning are usually connected and observed together. Recently Cesare et al. (2019) substantiated tetragonal symmetry for garnets with twin sector zoning, however, the sectors were not correlated to chemical discontinuities. Contrastingly textural sector-zoning, which is reflected by intragranular microstructures and inclusion fabrics, has been reported to occur independently of the other two sector zoning types.

2.2. Terminology of inclusion microstructures

A uniform terminology of microstructural features is essential for describing textural sector zoning. Rice et al. (2006) distinguished four different types of inclusions and intergrowths in sector-zoned garnets, based on observations with various samples and rock types, in combination with results from earlier studies (Andersen, 1984; Burton, 1986; Rice and Mitchell, 1991).

- **Type-1 inclusion:** Inclusions of quartz, Fe/Ti-oxides and graphite are found preferentially along sector boundaries and were derived from the rock matrix. Type-1 inclusions are relics of the rock matrix which were preferentially overgrown and enclosed by the garnet along directions, where the host crystal had grew not only radially, but also laterally to form a polyhedral crystal. This inclusion type has been inferred to be associated with rapid garnet growth during prograde metamorphism (Andersen, 1984; Burton, 1986).

- **Type-2 intergrowth:** Tubular, cylindrical inclusions of quartz, which are not relics of the matrix, but have formed syngenetically with garnet. Type-2 intergrowths originate at sector boundaries of the host crystal, and their long axis aligns to the growth direction of garnet. Burton (1986) reported quartz tubes that extend in a direction normal to the $\{110\}_{Grt}$ crystal faces. In this example, some tubes are not perfectly straight but curved, although each tube shows uniform extinction in OM, demonstrating that each tube consists of a single crystal with continuous lattice.

- **Type-3 inclusion:** Trails of abundant rutile inclusions occur parallel to Type-2 intergrowth or in a range of orientations sub normal to the pyramid base of $\{110\}_{Grt}$ or $\{112\}_{Grt}$ facets. The shapes of the inclusions constituting the trails vary between tabular, needles (with low aspect ratio) and equidimensional. The latter geometry is most prominent and defines this inclusion type. The spacing between Type-3 trail-inclusions is less than the thickness of the thin-section, since they are frequently observed passing over/under each other in OM (Rice et al., 2006).

- **Type-4 intergrowth:** Extremely thin, invariably straight and uniformly thick elongated rods can occur across the whole sector zoned garnet. Characteristically, their shape has a high aspect ratio and their shape preferred orientation (SPO) is related to crystallographic axes of the garnet host. Type-4 intergrowths do not reflect textural sector-zoning as such (Rice et al., 2006).

For all those types of inclusion microstructures different hypotheses have developed to explain the their formation. A selection on which is described in chapter 2.5.

2.3. Shape orientation relationships (SOR) of rutile inclusions and garnet host

Based on the terminology of inclusion microstructures in garnet by Rice et al. (2006), Type-4 intergrowths can have shape preferred orientations (SPO) parallel to four individual directions. These are parallel to the A_4 rotational axes of garnet. In other studies, Type-4 intergrowths were determined as rutile needles with their long axes strictly aligned parallel to $< 111 >_{Grt}$ directions (Hwang et al., 2007b, 2016, 2019; Griffiths et al., 2016, 2020; Guinel and Norton, 2006). These needles are considerably longer and more frequent than another set of less abundant SPO directions, which were found parallel to $< 100 >_{Grt}$ (Griffiths et al., 2020). Proyer et al. (2013) studied Type-4 intergrowths of rutile inclusions in garnet host in a similar sample (*2R5*) from the Xanthi complex. U-stage measurements indicate the alignment of dominant sets of Type-4 rutile needles parallel to $< 111 >_{Grt}$ and the subordinate sets parallel to $< 100 >_{Grt}$.

2.4. Crystallographic orientation relationship (COR)

The mineral inclusions in garnet studied by Griffiths et al. (2020) show various types of crystallographic orientation relationship (COR) to their garnet host lattice. These CORs possibly are controlled by a combination of different factors (intersecting symmetries, interface energy, strain energy, and crystal chemical factors). In recent years, the use of large orientation data sets gained from EBSD analysis and crystallographic relations gained from TEM, conjoined with microstructural observations of the inclusions, allowed to identify and classify axial relationships and CORs of rutile inclusions and their garnet host crystal (Proyer et al., 2013; Griffiths et al., 2016, 2020; Keller and Ague, 2019; Hwang et al., 2007b, 2015, 2016).
According to Habler and Griffiths (2017) *"specific"* CORs denote those, where the crystallographic orientations of the inclusions are fixed with respect to the host lattice, and variations of the inclusion orientations only reflect symmetrically equivalents of the same COR. Another type are *"statistical"* CORs, which describe the inclusions' orientations either to host planes with a rotational feature, dispersed around host axes, or combinations of both. Those *"statistical"* CORs have one or two degrees of freedom with respect to the host, but still reflect host crystal symmetry.
The current nomenclature for crystallographic oriented relationships (in the system rutile inclusions in garnet host) is not yet definite. Hwang et al. (2015) number the COR they observed by TEM analysis (*COR 1, COR2, COR2', etc...*), Griffiths et al. (2016) divide the COR groups based on the alignment of the $< 001 >_{Rt}$ directions with different directions in garnet (*R1, R2, R3, RX*; tab 1. in their publication). But both nomenclatures label only part of possible crystallographic orientation combinations. Griffiths et al. (2020) categorized large EBSD-orientation data sets by axial relationships between host and inclusion. The relationships therein are labelled according to the preceding studies. Derived from their classification script, a terminology by letter (e.g.: *RA, RAi, RAii, RB,... RX*) describes axial relation groups and specific CORs within those groups (see appendix A.3). However, not all CORs in this classification are proven to show a statistical relevance for the rutile-garnet system.

2.5. Hypotheses on the origin of inclusion microstructures

Whilst the trapping mechanism for Type-1 inclusions along sector boundaries is broadly accepted, the formation mechanism of Type-2 intergrowths is in discussion. Andersen (1984) suggested rapid garnet crystal growth involving the formation of screw dislocations in the host crystal, along which the cellular inclusions of quartz formed. Based on estimates of the oxygen fugacity in graphitic pelites, Burton (1986) suggested that the low solubility of SiO_2 in carbon saturated fluids induces an excess of SiO_2 at the propagating garnet growth facet, which caused incorporation of quartz in the growing garnet in the form of tubular intergrowth. However, quartz needs not be "in excess" to be formed as a phase. It can just derive from the reaction of porphyroblastic forming of garnet. Although, the lattice continuity of the quartz inclusions shows that new material was

added to the front of the growing crystal face according to the propagation direction of the garnet crystal. Another aspect discussed by Rice and Mitchell (1991) is the possible nucleation of Type-2 intergrowths at the surface of Type-1 inclusions, which further crystallise with a preferred growth direction parallel to a crystal orientation of the host.

Rice et al. (2006) observed variations in Type-3 inclusions and states that in most cases those trails are linear and clearly define a fabric of textural sector-zoning, whilst in other cases they are curvilinear, with several deviating orientations within a single growth sector of garnet. The linear trails have been found in correlation with type-2 intergrowths, the curvilinear trails with type-4 intergrowths. Andersen (1984) regards the Type-3 inclusions as remnants of the rock matrix in fast growing garnet domains, which would require chemical equilibrium between the trail inclusions and the rock matrix (Keller and Ague, 2019).
Other studies inferred the origin of trail inclusions are not associated with textural sector zoning and derived from healed micro fractures (Griffiths et al., 2014) or micro cleavages (Hwang et al., 2007a).

The origin of Type-4 intergrowths with a distinct shape orientation relative to the garnet host crystal is a hotly contested topic in the literature. Their formation by exsolution as a strictly intragranular mechanism has been rejected due to mass balance considerations. Exsolution of TiO_2 from stoichiometric garnet according to equation 2.1 (Hwang et al., 2007b) requires concomitant exsolution of pyroxene. Therefore, an open system mechanism has been suggested by Proyer et al. (2013).

$$\begin{gathered} M_3(MTi)Si_3O_{12} = TiO_2 + \frac{3}{2}(M_2Si_2O_6) \\ garnet = rutile + pyroxene \end{gathered} \tag{2.1}$$

Stöckhert et al. (1997) state that the internal structure of the poikiloblastic garnet reflects the distribution of preexisting mineral phases. This *hypothesis i)*, in which the Type-4 intergrowths are inherited by precursor minerals, like in the case of eclogitic metapelites from the Tauern Window in Stöckhert et al. (1997), was rejected by Proyer et al. (2013) for the Xanthi sample. In contrast, on the Tauern sample rutile formed from the TiO_2 content of mica replaced by garnet, and from rutile needles in sagenitic biotite. Still, the hexagonal sagenitic network and the rutile needle SPOs do not match the cubic garnet crystal structure. It is unclear why rutile needles lie specifically along the $< 100 >_{Grt}$ and $< 111 >_{Grt}$. However, external processes can not explain this phenomenon.
Hwang et al. (2007b) deploy the *hypothesis ii)* of cleaving and healing of garnet with rutile deposition forming Type-4 intergrowths. This approach includes the SPO formation of rutile parallel to the $< 111 >_{Grt}$ directions, which is referred to channels in the garnet structure that might be energetically/kinetically favoured sites for the nucleation and growth of rutile crystals. The source of Ti could be internal and/or external to the garnet host. Cleaving–healing is supposed to take place under very high P–T environments, in which a thermal or compressibility mismatch between inclusions and garnet host could

introduce minor cracks. This scenario may be relevant for the material investigated by Hwang et al. (2007b), which shows interaction of garnet with a melt phase. Contrastingly, the intragranular microstructures in garnet of the Xanthi metapelite do not comply with microcracking (Proyer et al., 2013).
Proyer et al. (2013) listed possible formation mechanisms for rutile intergrowth in garnet. Their *hypothesis iii)*, based on open system precipitation (OSP), combines the complex crystallographic and shape orientation relationships between garnet and rutile with potential mass balanced chemical reactions that can produce a TiO_2 phase by exsolution from garnet. The authors conclude that the observed abundance of rutile in garnet cannot form by exsolution from stoichiometric garnet under closed-system conditions. They infer that component exchange between the garnet interior and the rock matrix is required. Solid-state diffusion requires pathways for transport, like dislocations, nanotubes or subgrain boundaries.
Several hypotheses of origins for rutile needles with SPO in garnet were listed by Keller and Ague (2019, table 1). Still, unequivocal indicators for the identification on any definite formation mechanism is not yet generally available. Large multi-methodical data sets, which correlate the microstructural, textural and compositional features of the garnet host with the nature and the distribution of the inclusions are needed to identify indicators of particular formation mechanisms, and to test the various proposed hypotheses of inclusion origin.

3. Methods

3.1. Optical microscopy (OM)

From the rock sample XA-GO-1E a series of thin sections were prepared for optical microscopy (OM), see in figure 3 and appendix A.1. With the use of a Leitz Orthoplan, a Leica DM 4500p with a Zeiss Axiocam 208 (C-Mount, 0.55x) and *Zen software*, as well as a thin section scanner, the mineralogical composition of the matrix, and the inclusions in garnet were studied. Microstructural domains in garnet and associated inclusions were identified. Inclusions with particular shape preferred orientations (SPO) were counted in selected domains of the host crystal.

3.2. SPO frequency statistics

The aim of analysing SPO frequencies was to find correlation between the occurrence of different microfabrics associated with different facets and domains of the garnet host. Selected area, microstructural domain and facet orientation were taken in account. Three approaches for SPO counting were considered to master the following issues: which inclusion will appear in the statistic? Which inclusion will validate a shape preferred orientation?
The first approach employs the “Directionality” tool in image processing program *ImageJ* (1.53t). This approach allowed a quick confirmation of the main SPO directions. However, every grey value in the image, including cracks etc., and pixel related artefacts spoiled the quantification and returned an ordinate of no usable unit.
The second automated approach is based on plenty of image processing and the usage of the "Analyze Particles..." tool in *ImageJ*. In this case the colour threshold of an area (reduced in size to avoid cracks) was set to comprise only the inclusions in garnet. The SPO directions and frequencies gained by automated particle counting can be statistically evaluated for selected direction bins in *Excel*.
Both automated approaches resulted in a strong background noise and are highly sensible for pixel based artefacts. Therefore, the manual, third approach of marking each SPO inclusion in graphics editing software *InkScape* seems to yield the most reliable results. The human threshold for grey value and aspect ratio seems most correct. The number of marked inclusions can be exported to values of statistical importance.
To guarantee a constant information gain the OM images were taken as image stacks. The first photo is taken in focus on the surface, the next four images with a step size of $2\mu m$ in depth to determine the needle dip (optical parameters on Leica DM4500p: AP 38, FD 33 for minimal focus depth).

The dip can be calculated by

$$dip = \tan^{-1} \frac{n}{m}$$
$$\text{with} \quad n = (\text{Amount of images the SPO feature is in focus} - 1) * 2\,\mu m \tag{3.1}$$
$$\text{and} \quad m = \text{measured distance of SPO as a projection in a single image.}$$

Although, the calculated dip angles are afflicted with some uncertainty, due to optical distortion, the estimated angles from image stacks allow to infer the dip direction. This can be useful to generate a model of a garnet crystal orientation, when the garnet crystal orientation is unknown, assumed that type-4 needles indeed have elongation direction parallel to common garnet directions, as are $< 111 >_{Grt}$ and $< 100 >_{Grt}$.

For the highest statistical number all five images from the stack were combined in an *ImageJ* "Z-project" with minimum intensities. On Sample XA-GO-1E_II SPOs were manually counted in 8 areas, each with pairs of different garnet domains (Fig.: 14).

3.3. SPO modeling from OM images

From the SPO directions the orientation of the thin section plane can be obtained. In *SingleCrystal* (Version 2.3.1) the stereographic projection of Ia-3d was oriented, so the SPO directions fit. The high frequency SPO1-4 were considered to align along $< 111 >_{Grt}$, as revealed in recent studies (see chapter 2.3). The resulting viewing direction [uvw] resembles the pole of the (hkl) thin section plane. Using the software *Vesta* (Version 3.5.7 Momma and Izumi, 2011) a cut-model of the thin section plane and the garnet facets ($\{110\}_{Grt}$ and $\{112\}_{Grt}$) were obtained. The distances (d) of those planes, relative to the centre of the model, are variable: d(110), d(112), d(cut) were set in a way, that the cut-model equals the trace of garnet facets in the thin section. From this facet model of the host garnet crystal areas for SPO analysis were selected.

3.4. Micro computed tomography (micro-CT)

Computed tomography (CT) is used as a non-destructive technique to visualize and study external and internal structures of objects of remarkably different mass density. The Department of Paleontology at the University of Vienna holds a state-of-the-art desktop micro-computed tomography device (Bruker/Skyscan 1173).
The sample studied was cut from the hand specimen and shows an idiomorph garnet on the surface. The aim of micro-CT in this case was to find idiomorphic garnet facets of good quality, so they can be cut orthogonally for thin section preparation. To determine the internal structure and hidden habit of the garnet the sample was micro-CT scanned with an X-Ray beam at $130kV$. An average of eight frames were taken under the rotation step of 0.2°, resulting in a total of 1470 images with a voxel size of $18.956\mu m$. The raw images were handled as image stack.

The software packages *ImageJ* and *Amira* (5.4.1) were used to process and visualize the data. To reduce the data size the colour depth was set to 8bit, then rotated, that the corners of the rock chip are aligned with the image frame. The image stack was cropped, and only slides with data of interest were processed. The dimensions of the hand specimen refer to the axes in figure 2 c). Whilst half of the garnet was hidden in the bulk, the other half was on free air. This results in a brightness gradient in the images due to different radiodensity of air and the rock sample. After reslicing the image stack and applying the process "Enhance Contrast..." the contrast over the whole garnet was levelled.
Further processing included the segmentation of the bulk data into separate rock matrix-, garnet-, and quartz in garnet- data sets. First a median filter (2px) conserves the edges. Bloating the grey scale in brightness and contrast improves the execution of the *WEKA* segmentation plugin (Version 3.9.4, Arganda-Carreras et al., 2017) in *ImageJ*: the main goal of this plugin is to work as a bridge between Machine Learning and Image Processing fields. It provides the framework to use any available classifier to perform image segmentation based on pixel classification.
The plugin works by training a classifier for each phase of interest on only a few image slides. This means one classifier was trained for garnet to separate it from the matrix and one classifier for the internal framework of quartz in garnet. The plugin applies those trained classifiers on whole image stacks.
The *Amira* software can visualize the resulting segmented data sets in a "Multi-planar viewer". After translation of the data sets, they are displayed simultaneously as a 3D model and in three planar views, orthogonal to each other and free to move with this restriction.

3.5. Sample preparation based on micro-CT analysis

The segmented data resolved facets of visible quality. A particular $\{110\}_{Grt}$ facet was better accessible for a perpendicular cut (relating to the bulk´s edges for mounting on the diamond wire saw). The distances and angles relative to the bulk's edges were determined in *ImageJ*. The cutting plane was marked with tape and micro markings were drilled along the tape using a Dremel rotary tool. To reduce the cutting width the excess bulk containing only rock matrix was cut off with a diamond cutting disc. The final cut was done with a 30µm diamond wire and left two halves of garnet from which each a thin section was prepared.

3.6. Raman spectroscopy

Raman spectroscopy visualizes internal vibrations of matter by inelastically scattered light, which were all analysed on a Horiba Jobin Yvon LabRAM-HR, confocal micro-Raman system with 532/633 nm laser excitation at the Department of Mineralogy and Crystallography, University Vienna.
The investigation was focused on phase identification, Raman spectroscopy on carbonaceous material (RSCM) and Raman spectroscopy on quartz inclusions (RSQI). The choice of excitation laser and grating (600 or 1800) depended on the particular material, as well as the acquisition and filter parameters. The other machine settings remained constant for all measurements: objective with 50x magnification, slit $100\mu m$ and hole $300\mu m$. For processing the spectra *CrystalSleuth* (Version May 19, 2008) was used for background subtraction and comparison with reference spectra. *MagicPlot Pro* (2.9.2) serves for band fitting and for visualization of the spectra.

3.6.1. Phase identification

The vibration spectra gained from Raman spectrometry (RS) are characteristic for chemical bonds and help to identify phases relative to known references. This so-called *finger printing / indexing* identifies unknown phases in thin sections. The RRUFF database, as well as spectra of known phases serve as reference.

3.6.2. Carbonaceous material thermometry (RSCM)

Besides indexing, Raman spectra hold information about the state of order in carbonaceous material (CM). Based on the Raman shifts ($\Delta\tilde{\nu}$) of the D1, D2, and G modes of graphite, Beyssac et al. (2002) drew the linear correlation between the order of CM and the graphitization temperature.

$$\begin{aligned} R2 &= D1/(G + D1 + D2) \\ T[°C] &= -445R2 + 641 \end{aligned} \tag{3.2}$$

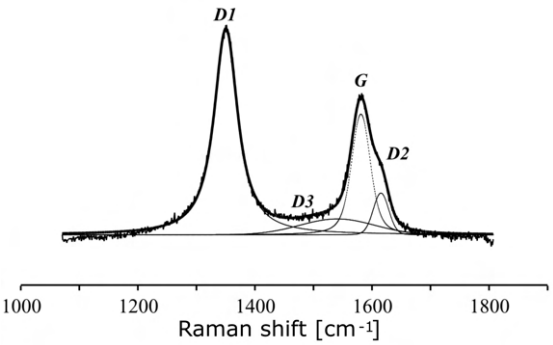

Figure 4.: Decomposition example of a Raman spectrum for first-order region of graphite, modified after Beyssac et al. (2002).

The resulting temperature has an accuracy of $\pm 50°C$ in a range of $330 - 650\,°C$.
The CM was excited with both a 532 nm and 633 nm laser. The spectra were recorded from Raman shift $\Delta\tilde{\nu}= 20 - 4000\,cm^{-1}$ to also observe presence of $O - H$ bonds. For the RSCM method only the D1, D2 and G vibrations are relevant, so only this range was band fitted in *MagicPlot Pro*. The first order band positions as shown in figure 4 were used in calculation 3.2.

Band broadening or full width-half maximum data (FWHM) hold further information about the ordering of CM but was not investigated in more detail.

3.6.3. Residual stress barometry in quartz inclusions (RSQI)

In addition to temperature, the residual pressure can also be estimated using Raman spectroscopy (RSQI). Internal stress of quartz and the correlating shift in wavenumber depend on pressure. The empirical approach of Hemley (1987) enables estimating residual pressures through numerical values of wavenumber shifts. For this method the Raman shifts of many vibration modes play a role.

$$P = (\nu_{stress} - \nu_{relax})\Delta\tilde{\nu}/dP \tag{3.3}$$

The numerical values for the pressure shift $\Delta\tilde{\nu}/dP$ were experimentally determined by Hemley (1987).
In geological samples, the reference for relaxed quartz is measured on quartz, which lays open on the thin section´s surface. Quartz inclusions, entrapped in other mineral host phases, remain with internal stress. The wavenumber shifts from the ν_{128}, ν_{206} and ν_{464} bands were considered for this barometer.
Apart from this approach Ashley et al. (2014) published the *Matlab* script *QuIB Calc*, which is another RSQI barometer that depends also on temperature and the composition of the garnet host based on the studies of Schmidt and Ziemann (2000) and Enami et al. (2007).
This barometer only involves the ν_{464} vibration's Raman shift, because its band has the highest intensity and the narrowest width, making band fitting and determination of the absolute x0 position the most accurate (Ashley et al., 2014). The results from chapter 3.6.2 (RSCM) were used as temperature input, whereas compositional data by Proyer et al. (2013) were taken as input for the garnet major element composition. The ν_{464} was determined by band fitting in a range of $\Delta\tilde{\nu}= 420 - 530 cm^{-1}$ with Lorentz and Gauss curves since the Software *MagicPlot Pro* (2.9.2) does not allow Pseudo-Voigt fitting.
Tomioka et al. (2022) proved the approach from Schmidt and Ziemann (2000) and Enami et al. (2007) works for quartz inclusions in kyanite hosts. The software *EosFit-Pinc* (Angel et al., 2017b) is a dedicated tool for elastic geothermobarometry by determining entrapment conditions from the measured residual pressure and Equations of State of minerals. With the excess pressures exhibited by mineral inclusions, trapped inside host minerals, metamorphic conditions can be determined. EosFit-Pinc calculates the isomeke, which is the line of constant relative volume of the inclusion phase and the host phase in P/T space, thus describing the relative volumetric changes of the involved phases with changing ambient conditions. With the input of the estimated residual stress in the inclusions and of the stress on the host at atmospheric pressure, both at ambient temperature, the isomeke plots along a P/T path, calculated with the Equations of State. The non-linear Equation of State data files used for the calculation of quartz inclusions in garnet host are from Angel (Alm: Angel et al. (2022), Qz: Angel et al. (2017a)). The kyanite data was from Nestola et al. (2018).

3.7. Scanning electron microscopy (SEM)

3.7.1. Sample preparation

The thin section XA-GO-1E_II was prepared for SEM by an additional chemo–mechanical polishing step with colloidal silica suspension (pH 9.2–10) as polishing medium on a rotary polisher. To establish electrical conductivity, a very thin carbon coating of the sample surface is necessary for EBSD analyses, which was archived by using a single carbon thread at vacuum conditions of $< 1 * 10^{-5} mbar$ during evaporation. On the thin section's edges a carbon paste was added to minimize charging of the thin section during interaction with the electron beam.

3.7.2. FEI Quanta 3D FEG-SEM

Sample XA-GO-1E_II was investigated in two analytical sessions on an FEI Quanta 3D field emission gun (FEG)-SEM at the laboratory for scanning electron microscopy and focused ion beam applications of the Faculty of Geosciences, Geography and Astronomy at the University of Vienna.
In the first session secondary electron (SE), backscattered electron (BSE) and forward scattered electron (FSD) images as well as EDX (energy dispersive X-ray spectroscopy) and EBSD (electron backscatter diffraction) analyses on garnet were collected. The session's focus was to determine the orientation of the host garnet and of its microstructural domains, identify corientation variations within the host crystal, to analyse the major element composition of garnet, inclusions and phases of the rock matrix by EDX. For BSE/SE/FSD imaging and EDX analysis a working distance (WD) of 10 mm was set. The accelerating voltage was $U_A = 15kV$.
Some selected domains were considered for further investigation due to their microstructural features. Overview images (BSE/SE/FSD) from this selection were stitched together manually (FSD) or automatically (BSE/ETD) using *ImageJ* and *Image Composite Editor* (Version 2.0.3.0).
From the collected overview images, analyses of the second session were focused on the rutile inclusions. Their crystallographic orientation was measured by EBSD, neighbouring phases were identified based on their major element content using EDX. In total, 582 EBSD spot analyses were collected in four areas of the host garnet (Fig.: 14).
EBSD analyses have been performed at a working distance of 14 mm and a 69.7° tilt of the section, yielding a beam incidence angle of 20.3° with respect to the sample surface. The beam parameters were set to Analytical beam mode, 1 mm SEM aperture, $U_A = 15kV$, $I \approx 4nA$. The Hough- and camera parameters, as well as the reference crystal structures (listed in appendix A.2) resulted in a solid automated band recognition and indexing (at an interplanar angle tolerance of 2°). Only 4% of the patterns had to be indexed manually.

3.7.3. EBSD data processing

The OIM^{TM} *Data Collection* software (Version 7.3.1) and the *mTex* plugin (Version 5.8.1, Bachmann et al., 2010) for *Matlab* have been used for data processing. In *mTex*, the data is first filtered by phase, twins and duplicates. For further investigation the orientations were handled *i)* in their original orientation in the thin section reference frame, or *ii)* normalised to the mean garnet orientation. The *i)* original data plots orientations relative to the sample and the SPOs within. The *ii)* normalised data rotates some crystallographic equivalent directions, which does not affect further COR classification of host and inclusion but the relation with the sample coordinates is lost. Each measured EBSD area was handled as unique to eliminate error in the mean of all garnet orientations due to possible minor misorientations in the garnet single crystal. Pole figure plots display the orientation of selected data. All pole figures were plotted with antipodal symmetry, in an equal angle, upper hemisphere projection (unless stated otherwise). For facet analysis of the garnet host the proper hemisphere must be selected with caution. Density plots, also known as orientation distribution function (ODF), were used to observe orientation relations in the original data. A half-width (HW) of 5° worked best for all ODF-plots. The COR classification in *mTex* followed the flowchart in A.4. The idea of filtering axial relationships between the crystal orientations of inclusion and host was introduced by Griffiths et al. (2020). Their script was used for computing with some adaptions (angular thresholds, additional axial relations).

Additionally with the measured garnet orientations, the cutting plane for a facet model can be refined. The linear system of equation 3.4 for the misorientation between two vectors can be solved with equation 3.5. In hindsight of possible misorientations in the garnet single crystal, this equation solves the orientation between the mean garnet orientation and the viewing direction of the garnet, as followed in equation 3.6, in which the result *view* (hkl) corresponds to the thin section plane.

$$\mathrm{A} * \mathrm{x} = \mathrm{B} \tag{3.4}$$

$$\mathrm{x} = \mathrm{A} \setminus \mathrm{B} \tag{3.5}$$

$$\mathrm{view} = \mathrm{round}(\ \mathrm{mean}(\ \mathrm{garnet.orientations}) \setminus \mathrm{zvector}) \tag{3.6}$$

Still for the facet model this exact thin section cut-plane leaves no sound solution for the variables d(110), d(112) and d(cut), and have to be selected by trial and error until the cut model aligns with the trace of garnet facets in the thin section.

4. Results

4.1. Phase content

All thin sections of the Ky-Grt gneiss sample XA-GO-1E comprise a similar phase assembly of coarse grained poikiloblastic garnet in a medium grained rock matrix of quartz, muscovite, biotite, kyanite, plagioclase and graphite as major phases, chlorite, rutile and apatite as minor phases, and accessory tourmaline, zircon and REE-phosphates. Worthy of note is the absence of pyroxene. In all thin sections opaque (in optical microscropy) phases are present. Those were mostly determined as Fe-sulfides/-(hydro)oxides by Raman and EDX, but were not in focus of this study. Below, the microstructural and compositional characteristics of the major phases are described in detail.

4.1.1. Kyanite

All thin section contain kyanite, few crystals show kinking (Fig.: 5). Kyanite is distributed in the Qz-mica-rich matrix, and partly occurs in contact with garnet. Kyanite shows poikiloblastic microstructure with inclusions of quartz and graphite reflecting a foliation. Some of the kyanites' crystal boundaries are associated with REE-phosphates, observed from EDX.
In sample XA-GO-1E_III a single kyanite was observed incorporated in the garnet core, which dates the kyanite prior to or associated with the first garnet growth stage. Pressure estimation for the stage of kyanite growth is based on RSQI on quartz inclusions (see chapter 4.1.2).

4.1.2. Quartz

From optical microscopy five different generations of quartz were observed (Qz1-Qz5).

Quartz in Garnet

The first generation (Qz1) is present as polycrystalline bands alternating with layers of rutile and graphite in the garnet core. Compositional layering and shape preferred orientation of theseinclusion phases represents the earliest identified foliation that was intertectonically overgrown and enclosed by garnet during the first garnet growth stage. Along the Qz1 grain boundaries thin layers of garnet form a net like structure.
The second-generation quartz (Qz2) is the product of recrystallisation of former Qz1. The macro structural orientation follows the first foliation. Furthermore, Qz2 forms strain shadows around the garnet core, which were overgrown during the subsequent garnet

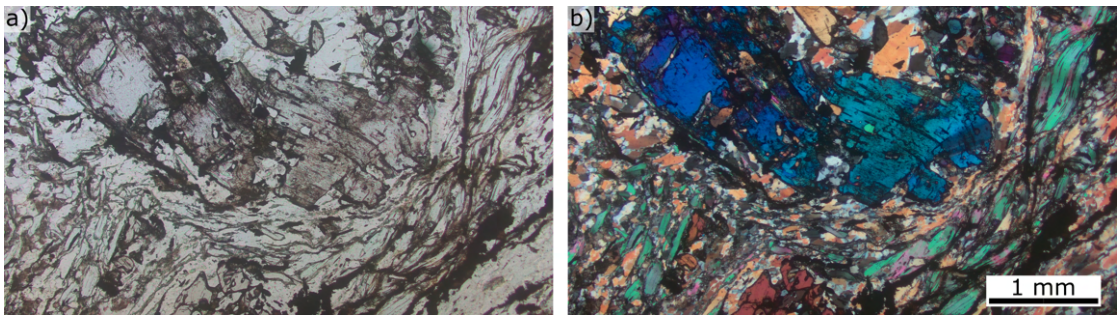

Figure 5.: a) Parallel polarised light, b) cross polarised light OM image of kyanite in rock matrix of thin section XA-GO-1E_A. Polikiloblastic texture, as well as kinking can be observed.

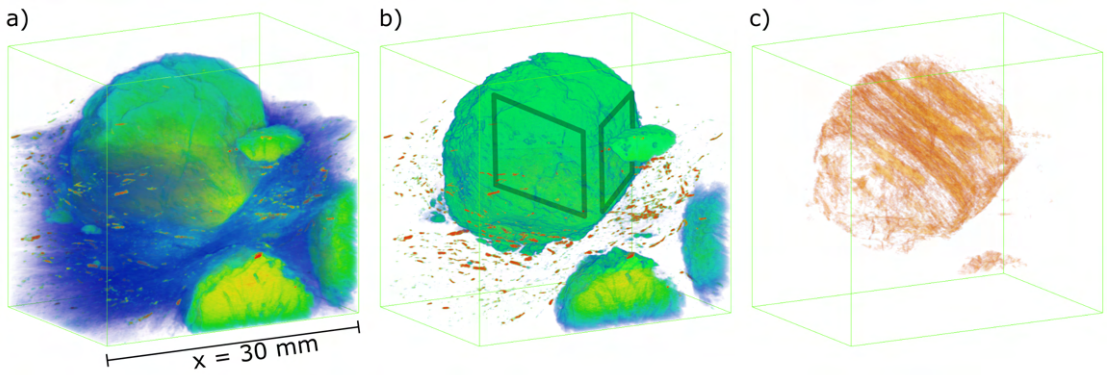

Figure 6.: Micro-CT model of rock chip from which thin sections XA-GO-1E_IIIa/b were extracted. On display are three models, generated in software *Amira*, in identical viewing position: a) showing multiple garnets embedded in the rock matrix. b) Only phases of high radiodensity are shown in the rock matrix. The garnet in focus forms macroscopic $\{110\}_{Grt}$ facets, marked with black outline. c) Look on the internal quartz foliation, which occupies a dominant part of the garnet.

Figure 7.: (Next page.) Inverse pole figure map (IPF map, reference direction A1, as inferred in c)) focusing on a) the garnet zones Grt1 and Grt2 in thin section XA-GO-1E_II. Local misorientations do not exceed 2°. Legends of IPF maps are given below. The location of the EBSD map scan is marked in figure 14.
b) IPF map of quartz: The SPO of Qz1 defines the first foliation, Qz2 represents a deformation shadow adjacent to Grt1. Qz3 enclosed in Grt2 has elliptical 2D geometry in the thin section plane. The Qz aggregate in the lower right is located at a sector boundary of garnet.
c) Harmonic texture plots (maximum density = 2.993, logarithmic increments) of quartz c- and a-axes show no distinct crystallographic preferred orientation.

growth stage. Qz2 also forms Type-1 inclusions, accumulating along sector boundaries within garnet. Barometry (chapter 3.6.3) based on Raman spectra of Qz2 inclusions and quartz along sector boundaries yielded a maximum estimated residual pressure of 0.22 GPa for the garnet core and 0.26 GPa for the outer garnet domain. The limited amount of analysed grains restricts these pressures to guide values, no further method for pressure estimation was applied.

The third generation quartz (Qz3) forms inclusions in garnet, classified as Type-2 intergrowth. They have tubular shape and the geometry of the 2D section is highly dependent on the thin section's cutting plane with respect to the garnet lattice and the associated SPO of the Qz3 tubes. If cut parallel to their elongation direction, Qz3 crystals have high aspect ratio in 2D section, else if cut perpendicular they have circular or elliptical 2D geometry. The tubular shape of Qz3 was confirmed by the micro-CT data. EBSD crystal orientation data (n=14) of these quartz intergrowths showed no COR between Qz3 and the garnet host crystal. Some Qz3 tubes show twinning according to Dauphiné law (60°, [0001]).

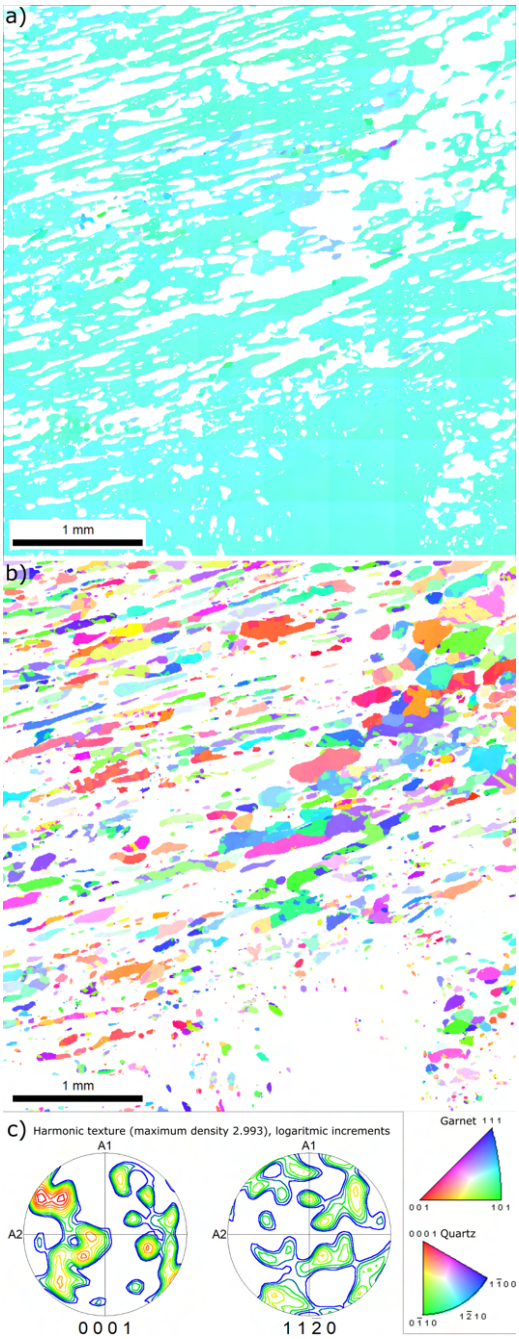

Figure 7.: (Caption previous page.)

Quartz in matrix

In all studied thin sections, apart from the quartz inclusions in garnet, phase boundaries between garnet and quartz of the surrounding rock matrix appear serrated, indicating a reaction relationship. Further quartz generations are restriced to the rock matrix, indicating that their microstructures postdate garnet growth. Qz4 is a product of recrystallisation during/after folding of the compositional layering, Qz5 shows dynamic recrystallisation by bulging in matrix domains, affected by localised shear zones. At rather low strain rates, microstructures of low temperature grain boundary migration indicate dynamic recrystallisation in an estimated temperature range of 450-550°C. Observed quartz fabrics are consistent with those reported by Krenn et al. (2008).

Quartz in Kyanite

Kyanite hosts spheroidal or ellipsoidal inclusions of quartz on which barometry was performed based on Raman analysis (RSQI). Applying an empirical approach (Hemley, 1987) yielded a maximum estimated residual pressure of 0.5 GPa, whereas a more a refined approach yielded 0.45 GPa (Schmidt and Ziemann, 2000; Enami et al., 2007; Tomioka et al., 2022).

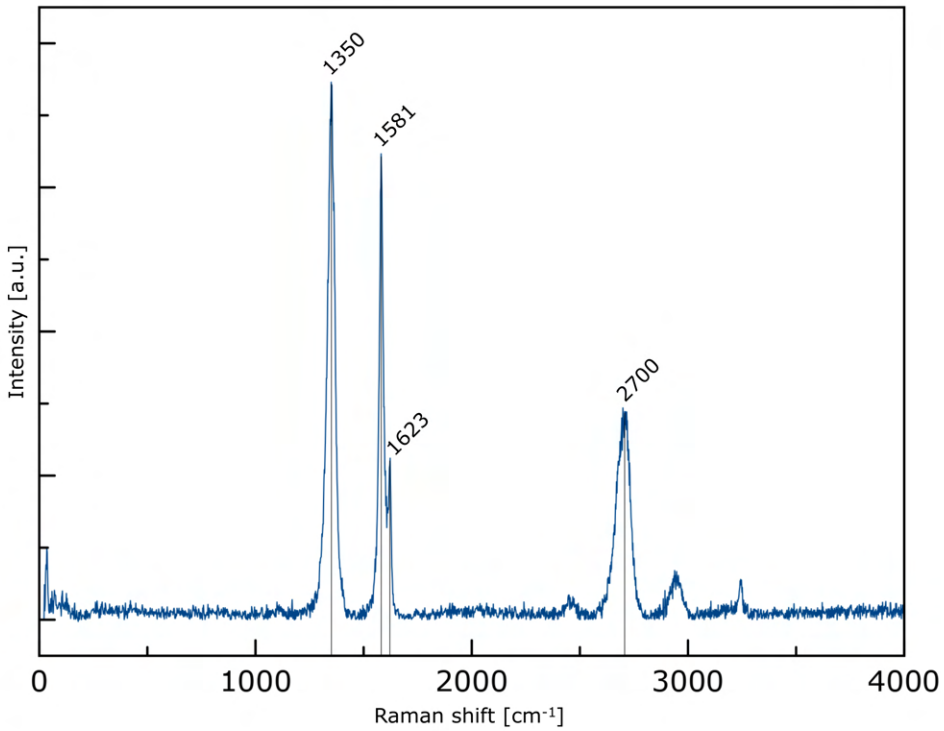

Figure 8.: Raman spectrum of a graphite, enclosed in the garnet core (Grt1), showing a shape preferred orientation parallel to the oldest observed foliation. The graphite was excited with a 532 nm laser, yielding in the first order D1, G and D2 bands at $\Delta\tilde{\nu}= 1200 - 1700 cm^{-1}$, as well as $O-H$ bands at $\Delta\tilde{\nu}> 2500 cm^{-1}$. Background subtraction applied in software *Crystal Sleuth*.

4.1.3. Mica

The dominant phyllosilicates are biotite and white mica, whereas chlorite is a late-stage alteration product. Based on EDX analysis muscovite was identified as the prominent white mica phase, although fine-grained paragonite is present in the rock matrix as well. White mica shows microstructurally different generations. The SPO of micas represents a foliation that was folded and deflected around the garnets, indicating shear deformation

that postdates the earlier garnet growth stages. The grain sizes vary strongly and range from $< 100\mu m$ to millimetre scale. Micas recrystallised in fold hinges, and partly were rotated parallel to fold axial planes.
Chlorite seems to replace biotite along cracks and the outermost part of garnets, as well as in the rock matrix.

4.1.4. Plagioclase

Plagioclase is present as $< 500\mu m$ sized crystals in the rock matrix. Partly, plagioclase appears altered to sericite. In optical microscopy (OM) plagioclase can be observed untwinned or shows polysynthetic twinning. Apart from twinning, EDX analysis shows orthoclase content of plagioclase below 1 mol% and changes in the anorthite content (in mole%) between the core (an22) and the rim (an31), see figure 9.

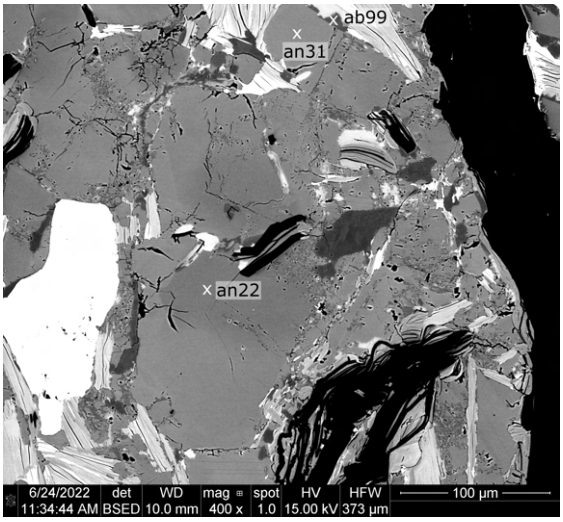

Figure 9.: BSE image of plagioclase (Pl) in rock matrix. Three EDX point measurements indicate changes in the Pl composition. The anorthite content increases from centre of the crystal (an22) to the rim (an31). The outermost part shows pure albite (ab99).

4.1.5. Graphite

In all thin sections graphite is present in the rock matrix, as well as enclosed in garnet. Graphite inclusions in garnet are associated with Qz1 reflecting in the earliest foliation, as well as with Qz3 tubes or with Qz2 found along sector boundaries of garnets. At the phase boundary of garnet with phases of the rock matrix graphite is foliated in association with micas and quartz, showing SPO with concentric arrangements around garnets. Graphite in the rock matrix has prolate geometry and shows SPO parallel to the main foliation of the rock matrix. Graphite frequently occurs as inclusion in quartz.
RSCM thermometry (chapter 3.6.2) yielded a temperature of $T = 510°C \pm 50°C$, equally for graphites located in matrix or garnet. The Raman spectra shows the significant broad D1 band at $\Delta\tilde{\nu}= 1340 - 1350cm^{-1}$, which is not included in the (RRUFF) reference spectra and must not be confused with a first order diamond band at $\Delta\tilde{\nu}= 1334cm^{-1}$. The similar band positions are attributed to a certain carbon structure within both minerals, graphite and diamond (Mposkos and Kostopoulos, 2001).

4.1.6. Garnet

The studied garnets from the Ky-Grt gneiss sample XA-GO-1E vary in diameter from 5-30 mm and show a remarkable inclusion zoning indicating different growth stages, as well as different states of preservation. Whereas, with the cutting effect in mind, some garnet crystals are idiomorphic and faceted, others show sutured phase boundary segments, especially adjacent to Qz, Bt and Pl, indicating a reaction relationship. In the 3D model, generated from the micro-CT data set of specimen XA-GO-1E_III, the garnet forms dominantly macroscopic $\{110\}_{Grt}$ facets with "rounded" facet junctions, which could represent subdominant $\{112\}_{Grt}$ facets (see Fig.: 6). This was also confirmed for specimen XA-GO-1E_II by EBSD crystal orientation data correlated with the orientation of boundary traces in OM images. A $\{110\}_{Grt}$ facet model generated from EBSD orientation data reveals the resulting facets cut by a $\{205\}_{Grt}$ plane fit with the facet trace of garnet in the thin section. The model includes facets on both the upper and lower hemispheres in pole figures plotted in the thin section coordinate system as for EBSD data collection (Fig.: 15). Additionally, the model also aligns with subdominant $\{112\}_{Grt}$ facets. While sector boundaries traced by Type-2 inclusions may hint potential facet junctions, they do not align consistently with the model. For simplification, the habit of garnet in the studied sample is assumed to be primarily composed of $\{110\}_{Grt}$ facets with rounded corners. These corners are made up of $\{110\}_{Grt}$ steps, which result in a $\{112\}_{Grt}$ trend for the subdominant garnet boundary segments.
Garnet of the studied Ky-Grt gneiss, as observed by Proyer et al. (2013), has an almandine composition, and shows concentric chemical zoning with increasing Mg-content towards the rim. EDX data from thin section XA-GO-1E_II qualitatively confirms this compositional trend.

4.2. Microstructural domains in garnet

All garnets in the studied thin sections show domains of microstructural sector zoning, which is reflected mainly by the arrangement of inclusions. The fact the garnet is composed dominantly by $\{110\}_{Grt}$ growth sectors is an evidence, that chemical sectoring is not present, subtle differences in composition between different sectors were not detected by EDX. Absence of birefringence in optical microscopy and absence of twinning confirmed by EBSD crystal orientation data of garnet reject twinning sectoring. Hence in the studied garnets sector zoning is defined exclusively by microstructural features. Further, based on the distribution, geometry and SPO of inclusions and intergrowths, all analysed garnets feature three main concentrically arranged microstructural zones. Throughout all zones Type-4 intergrowth of rutile needles with low aspect ratio (AR) are observed. They all follow a distinct SPO, further described in chapter 4.3.
The garnet core domain is characterised by a remarkably planar internal foliation reflected by Qz1 bands and the SPO of rutile and graphite, which were intertectonically overgrown during the first garnet growth stage. This poikiloblastic garnet zone is labelled Grt1 (Fig.: 10 a) b)). There, the Type-4 rutile needles mentioned above occur in low frequency.

In thin section XA-GO-1E_II this domain is clearly separated from the subsequent garnet growth zone by increased presence of Qz2 in the form of a deformation shadow (figure 14). Still EBSD crystal orientation measurements (single points/area scan) reveal no major crystallographic misorientation between those concentric zones, as shown in the EBSD map (Fig.: 7).

Grt2 is defined by tubular Qz3 with long axes aligned perpendicular to the corresponding garnet facet, and therefore supposedly parallel to the growth direction of garnet (Fig.: 10 c)). Some Qz3 tubes show curvature. Also, rutile inclusions with characteristic microfabrics reflecting sector zoning of garnet are present throughout this domain. In more detail Grt2 is divided into three subdomains: Grt2a is not concentric, rather shows axial appearance of Qz2 which represents a deformation shadow that developed during deformation postdating growth of Grt1 and predating Grt2 formation. In the data gained by micro-CT the network of Qz2 dominates the majority of the garnet XA-GO-1E_III, displayed in figure 6. Subdomain Grt2b (also referred to as *trail domain*) is defined by the presence of characteristic Type-3 inclusions of rutile. In this domain rutile occurs in two main habits: equant rutile with an approximated maximum diameter of $1\mu m$ or any smaller; and rutile needles with a rather low aspect ratio, which have a strong influence on the SPO frequency studies in chapter 4.4. In addition, tabular rutile inclusions appear in a minor frequency. Equant Type-3 inclusions form a trail fabric. The trail directions are subperpendicular to the corresponding garnet facet and thus parallel to the Qz3 tubes and the inferred growth direction of garnet. By correlation with the crystallographic orientation of garnet, gained from EBSD analysis, the trail directions were mostly parallel to $< 110 >_{Grt}$. Still, exceptions were observed, as some sites show multiple trail directions, and some trails extend along a $< 112 >_{Grt}$ instead of $< 110 >_{Grt}$. Some of the trails can not be directly related to the host symmetry. Supposedly these trails follow the prior foliation or cracks in garnet. Area9 (Fig.: 11) shows two trail directions. Their traces follow two different $< 110 >_{Grt}$ directions. The predominant trail direction correlates with the plane normal of the $\{110\}_{Grt}$ growth facet, whereas the subordinate trail direction correlates with another $< 110 >_{Grt}$.

In the subdomain Grt2c (also referred to as *needle domain*) Type-4 rutile intergrowths dominate the microstructural fabric. These needles vary in length and thickness, but tend to have a high aspect ratio. All needles pertain to a particular SOR and thus have a characterictic 3D arrangement in each host garnet. Subordinately, domain Grt2c also hosts trails. The transition between trail domain and needle domain is gradual. No hard interface between these domains was observed (Fig.: 10 d)).

Contrastingly, the outermost microstructural zone of garnet, labelled Grt3, is separated from Grt2 by a string of inclusions, consisting of graphite, rutile, or mica. The separating, interfacial inclusions represent an external foliation. The zone Grt3 itself is mostly optically free from inclusions (as observed in OM). This zone varies in thickness and may even be absent, but no direct correlation to neighbouring phases was identified.

Apart from these concentric zones of garnet, Type-1 inclusions trace sector boundaries between $\{110\}_{Grt}$ growth pyramids, which form the garnet's crystal shape (Rice et al., 2006). The Type-1 inclusions consist of quartz, rutile, graphite, iron sulfide and other polymineralic phases.

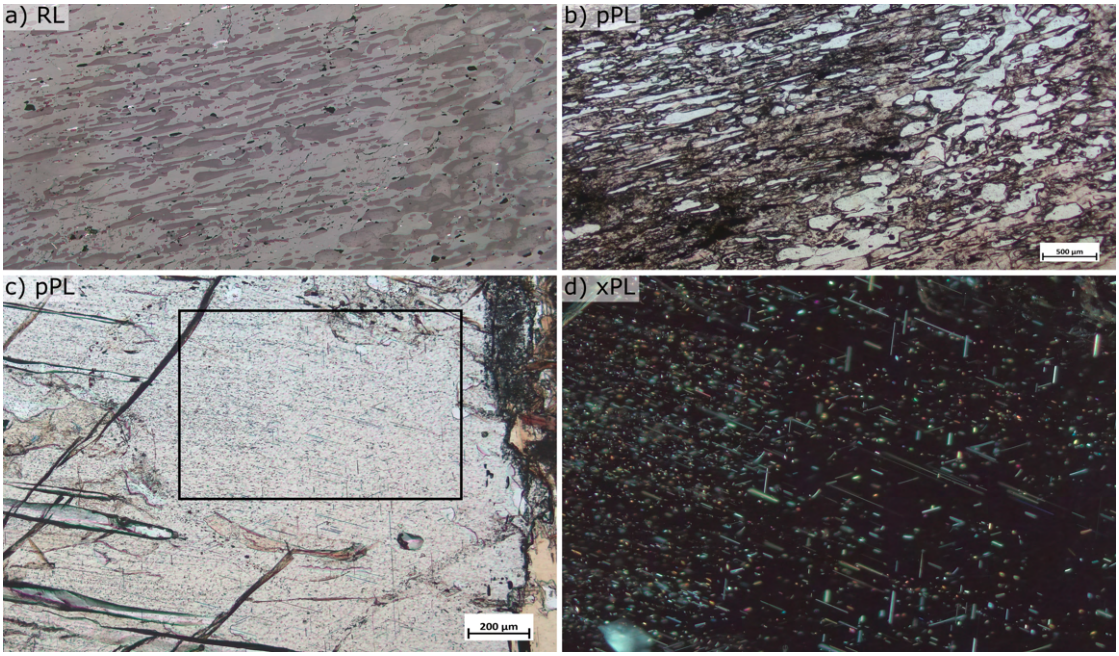

Figure 10.: a) Reflective light (RL) image of the garnet core, representing Grt1 with Qz1, rutile and graphite inclusions with SPO correlated with foliation, and Grt2a, which is defined by the appearance of Qz2, resembling a deformation shadow. b) Parallel polarised light (pPL) image of the same area. c) Grt2 is defined by tubular Qz3 intergrowth and is subdiveded into Grt2a, Grt2b (trail domain) and Grt2c (needle domain). The black rectangle indicates the area captured in d) with crossed polarised light (xPL). The microstructural difference between trail and needle domain of garnet is evident in this area.

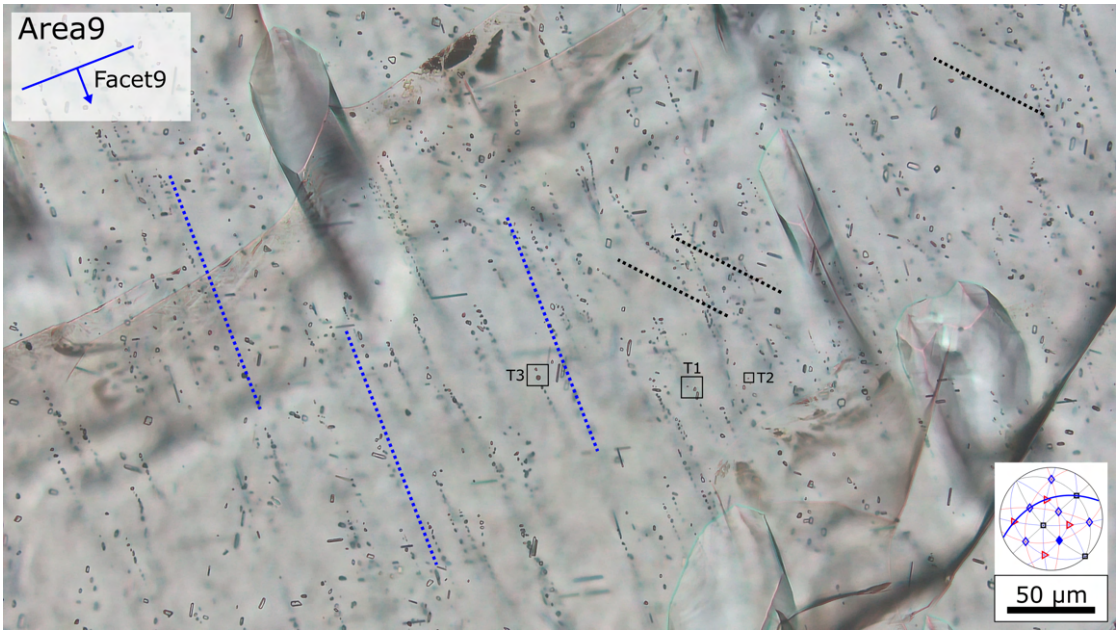

Figure 11.: Subsection Grt2b with domain defining Type-3 inclusion trails. Multiple trail directions are present. The blue trace corresponds to the $\{110\}_{Grt}$ growth facet, the black trace aligns with an different $< 110 >_{Grt}$ direction. Three specific areas (T1, T2 and T3) are marked in yellow, in each rutile twinning was observed. The location of Area9 and its correlating facet are marked on figure 14b).

While all garnets are single crystals, EBSD data reveals some slight misorientations ($< 2°$) over the length of the single garnet crystal of sample XA-GO-1E_II. These subtle intergranular misorientations are associated with deformation of garnet postdating garnet growth. Grain internal misorientations in garnet accumulate in domains with frequent quartz inclusions, where garnet only forms thin 'bridges' between inclusions, as shown in EBSD scan, figure 7. In some domains, the misorientations are connected with cracks. The deformation causing intragranular misorientations in garnet clearly overprints the formation of rutile inclusions, as the latter pin low angle boundaries in garnet, as observed in FSD imaging, figure 12.

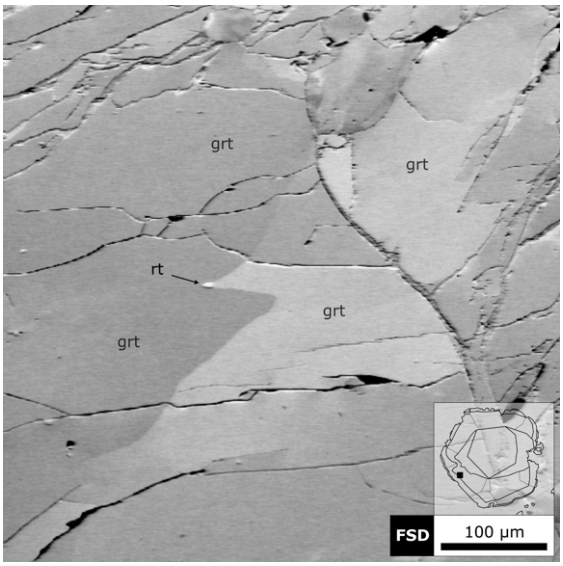

Figure 12.: Forward scattered electron (FSD) image of garnet XA-GO-1E_II with a visible orientation contrast in an else homogeneous garnet. The misorientation was measured to 2°. (The image location is indexed in an schematic overview of the garnet.)

4.3. Inclusions and SPO types

All studied garnets comprise inclusions of quartz, rutile, graphite, apatite, mica and Fe-sulphides/(hydro)oxides. Biotite was found along cracks in the garnet. White mica was observed entirely enclosed by the garnet lattice. The shape preferred orientation of quartz, rutile, graphite and apatite reflect the foliation present in Grt1, in which Fe-phases also occur. Additionally, these phases are aggregated along the sector boundaries of Grt2. Apart from their identification with Raman and EDX, these Type-1 inclusions were not studied any further.
In growth sectors of Grt2 quartz and rutile are identified as major inclusions. In thin section XA-GO-1E_II also a Ca/Mg-carbonate was found within the Grt2 host. In few cases kyanite (n=9, in one case kyanite & quartz) were determined in association with rutile inclusions, both Type-3 and Type-4, in Grt2. In one case apatite was found in association with a Type-3 rutile inclusion. Their sizes (observed in SEM imaging) were in the range of the rutile inclusion outcrops (ca. $1\mu m$).
Based on EDX-analysis, the phase associated with rutile in polymineralitic inclusions (n=9), were identified as a Zn-Al oxide phases. Supposedly this phase is Zn-spinel (gahnite), though establishing stoichiometric balance was impended by the mixed EDX signal, caused by the small crystal size.

In all domains and in particular the Grt2c domain rutile needles representing Type-4 intergrowths show shape preferred orientation throughout all thin sections. In all samples

4 to 6 different orientations of the rutile needle elongation direction were observed. In the 2D observation in OM rutile needles vary in thickness and length, although the latter can be a consequence of a section effect. The same SPO directions observed with Type-4 inclusions, were also identified with Type-3 inclusions constituting trails in Grt2b domains, by the automated approach of image analysing in *ImageJ*. Many of those low aspect ratio needles seem to emanate from inclusion trails, which is exemplary shown in Area1 (figure 16 on page 34).
EBSD analysis applied to garnet domains in thin section XA-GO-1E_II reveal the shape preferred orientation of rutile inclusions depends in fact on the crystallographic orientation of garnet. The most frequent shape preferred orientations of rutile needle long axes (SPO1-4) are parallel to $< 111 >_{Grt}$, whereas the subdominant SPO5 and SPO6, that are mainly reflected by rutile needles with a low aspect ratio, are parallel to $< 100 >_{Grt}$. The cubic equivalence of garnet symmetry implies a further possible $< 100 >_{Grt}$ direction (SPO7), which has not been found in the studied sample. Other SPO directions exist at vary low frequency thus were not studied in detail.
In further pole figures the $\{111\}_{Grt}$ plane poles are labelled according to the SPO directions of the rutile needles (e.g. figure 15, SPO1-4). In particular, the foliation of Grt1 in mind, SPO1 & SPO4 lie (close) within the foliation plane, which is observed only as trace in OM. Contrastingly, SPO2 & SPO3 are oriented at a rather high angle with respect to the foliation plane.
The directions of inclusion trails show orientation relationships with particular crystal planes of the hosting garnet. The preferred direction of inclusion trails correlate to the direction perpendicular to the corresponding $< 110 >_{Grt}$ facet. The facet normal direction is supposed to represent the growth direction of garnet, along which the trail of rutile inclusions are aligned. With respect to each $< 110 >_{Grt}$ growth direction, two certain $< 111 >_{Grt}$ are oriented at an angle of 35°, whereas the two other $< 111 >_{Grt}$ are at an angle of 90°. The latter are therefore parallel to the studied $\{110\}_{Grt}$ growth facet. This symmetric relation can be observed in the pole figures (e.g: Fig.: 15) and was also approved by calculation of the angular relationships in *mTex*.

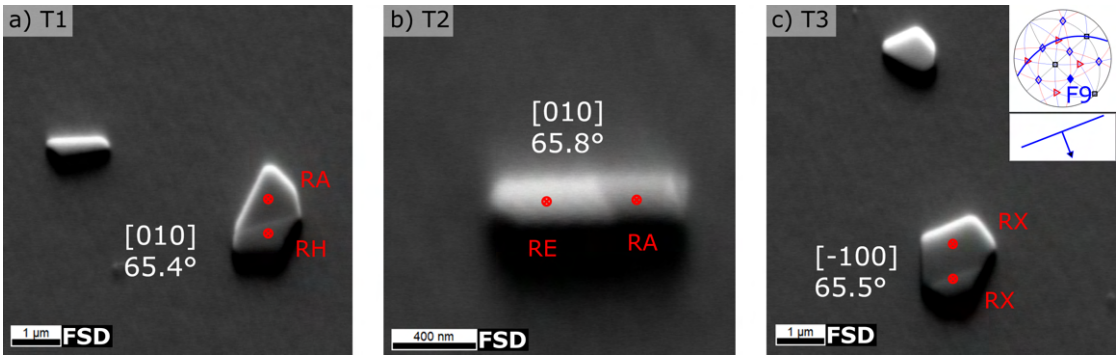

Figure 13.: Exemplary selection of rutile twins, observed in Area9 on FSD electron images. Their twin plane and angle was determined with calculation of EBSD single point measurements (red markings). For each twin two COR groups were classified (in red letters). Twin T3 was not sucessfully classified into any statistically (known) COR.

Further, ten rutile inclusions in Grt2b (trail domain) show twinning (7 equant-, 2 undefined-, 1 needle-rutile). Eight of those twinned rutile crystals show $\{101\}_{Rt}$ reflection planes with an average twinning angle of 65.5°, so called "elbow twins". Another "elbow twin" was observed with a twinning angle of 45.4°, its reflecting plane was not determinable. A third type of twinned rutile was found with a $\{301\}_{Rt}$ reflection plane and a 53.7° twinning angle. Those reflection planes most often align to the trail direction, either parallel or perpendicular to said direction, as indicated in figure 13.

4.4. SPO frequencies

SPO frequencies in thin section XA-GO-1E_II show characteristic differences when comparing data from different analysed areas (see all counted areas on figure 14 b) and counted frequencies on pages 34f). Most obvious is the difference between the needle domain and trail domain even within one growth sector. It is important to note that only the $< 111 >_{Grt}$ SPOs (1-4) are counted in a statistically significant amount, whereas the $< 100 >_{Grt}$ SPOs (5-6) are very rare in all studied domains/areas. Rutile inclusions of tabular habit do not appear in the SPO frequency study, due to their shape which prefers no observable orientation in the thin section.
Linking the SPO frequency statistics for needle and trail domains of each area allows for grouping the areas. Generally, in the Grt2c domain, where rutile needles form the dominant inclusion microstructure, the distribution of rutile needles with SPO1-4 is uniform (each amounts to 25%). This observation is consistent in half of the Type-4 intergrowth (needle domain) areas (Fig.: 16, page 34).
SPO frequencies of rutile inclusions in Area1 and Area2 (garnet growth sector of facet1, lower hemisphere) yielded a general result: whereas the rutile SPOs 1-4 are equally distributed in the needle domain, two SPO directions are dominant in the trail domain. There, SPO2 & SPO3 have a high frequency (>25%), while SPO1 & SPO4 are subdominant (<25%). Considering the trail direction and the orientation of the particular $\{110\}_{Grt}$ growth facet (facet1), the dominant SPOs are at a 35° angle with respect to the corresponding $< 110 >_{Grt}$ growth direction of garnet. The subdominant SPOs lie within the $\{110\}_{Grt}$ growth facet, and are marked with fine hatch pattern in figure 16 a), b). This trend is indeed reproducible, as seen in the varying sample sizes of SPO countings (Area1: n=160, Area2: n=96).
Area3 in the growth sector of facet2 (lower hemisphere) as well shows equal SPO distribution in the needle domain. In the trail domain, however, inclusion trails are aligned along either several $< 110 >_{Grt}$ or $< 112 >_{Grt}$. In this sector, the SPO frequency statistics for the trail domain show that only SPO3 is dominant. The SPO directions, which lie in the growth facet plane of garnet are SPO2 & SPO4. Additionally, $< 112 >_{Grt}$ trails indicate the proximity of Area3 to the sector boundary between the macroscopic $\{110\}_{Grt}$ growth sectors (facet2 and facet1), and a potential narrow $\{112\}_{Grt}$ growth sector. As observed in Area1, facet1 has particular favoured and subdominant SPO directions, which may influence the frequency of SPO1 in Area2 (Fig.: 16 c) coarse hatch pattern). The SPO distribution of rutile inclusions in the trail domain of facet2 seems

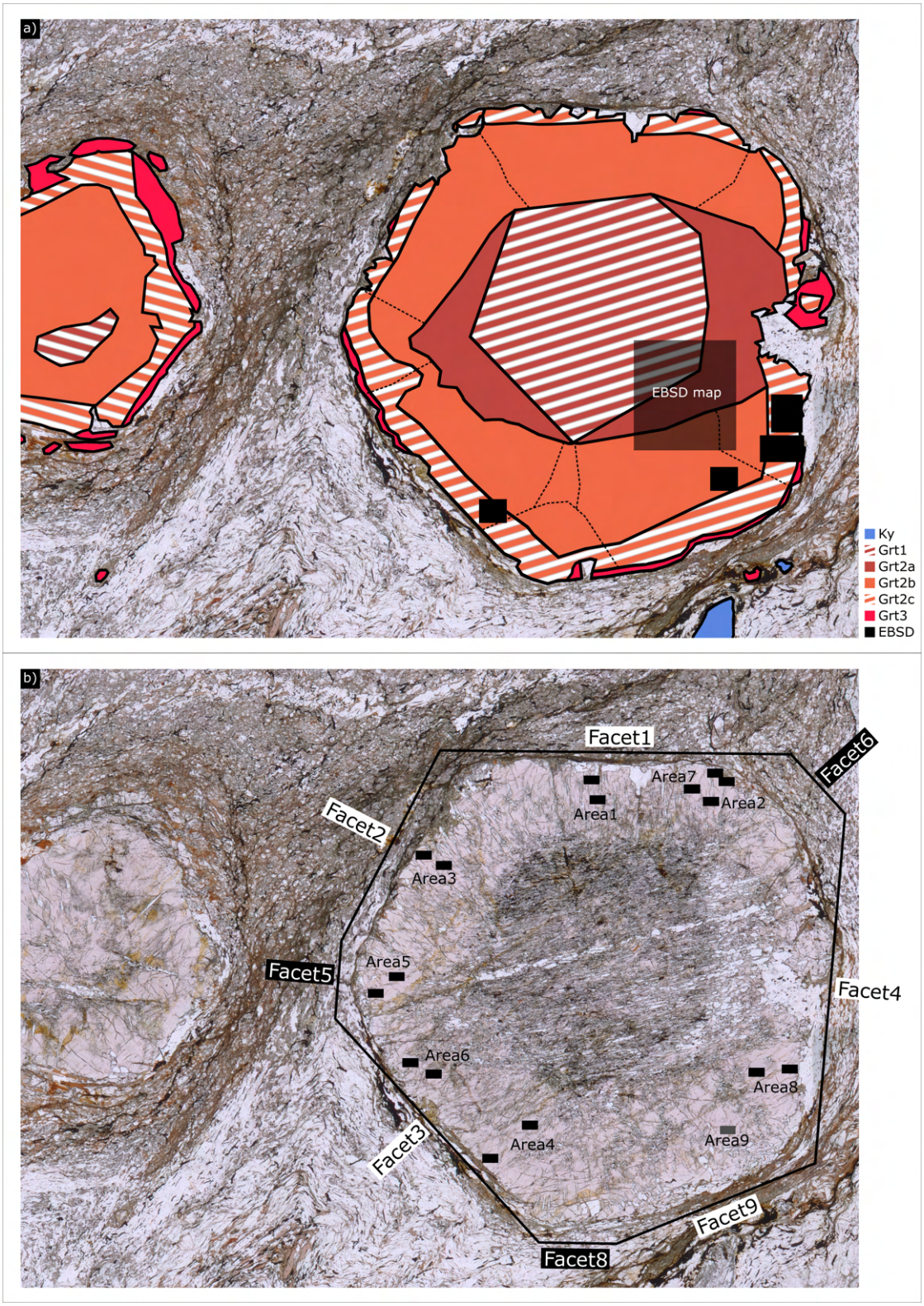

Figure 14.: Thin section scan of sample XA-GO-1E_II, diameter of labelled garnet crystal is 19 mm. a) Observed microstructural domains and areas of EBSD study. b) Pairs of Areas and facets, in which SPO frequencies were quantitatively analysed (Area1-8), an additional label for Area9/Facet9 indicates the area shown in figure 11 (no frequency data available). Overlayed are the traces of $\{110\}_{Grt}$ facets reconstructed from a crystal model based on EBSD orientation data. Facets1-4 are marked in white, their plane normal point to the lower hemisphere. Facets 5, 6, 8 marked in black have normal directions pointing into the upper hemisphere on the pole figure plots in Fig.: 15.

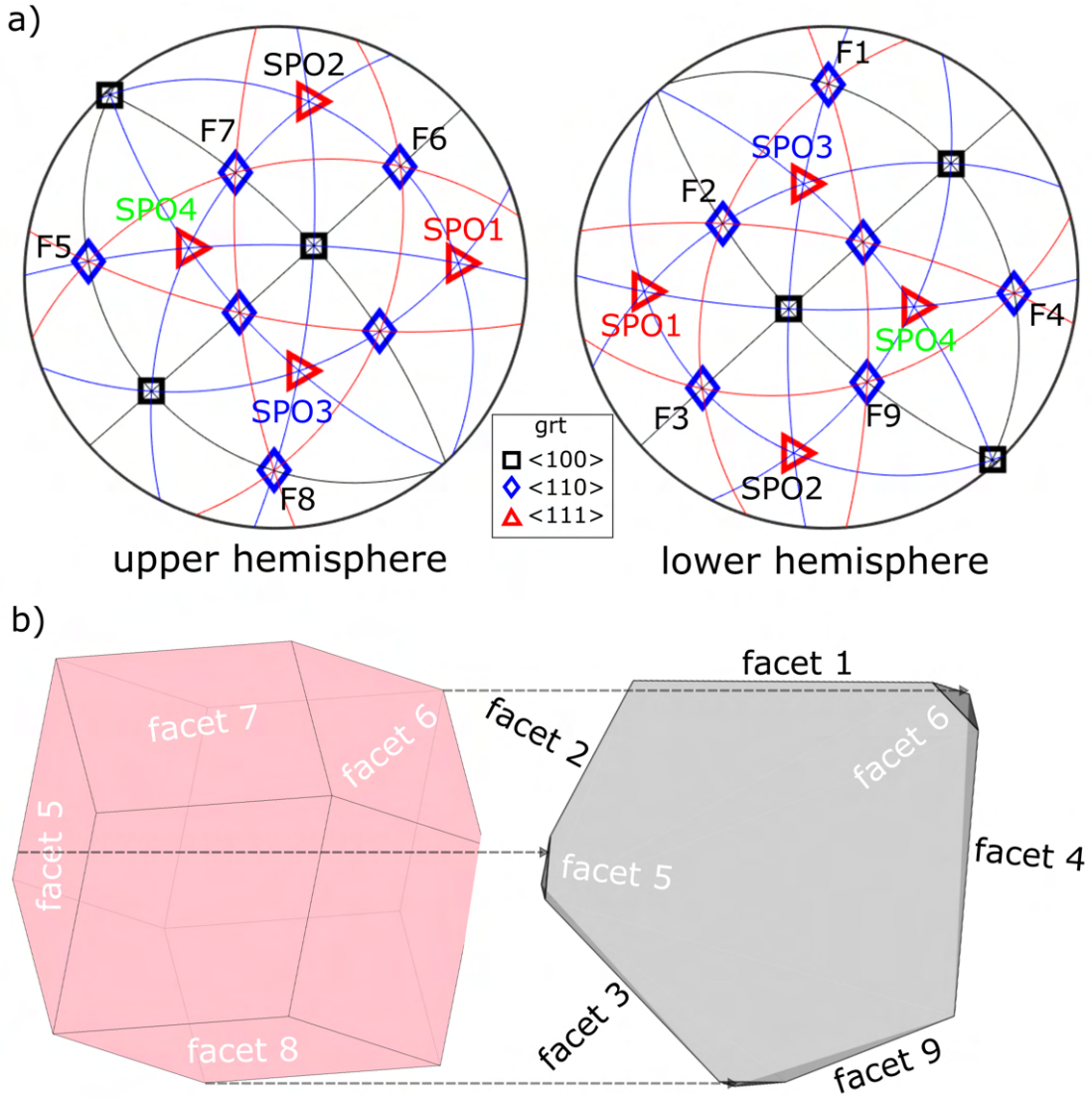

Figure 15.: a) Pole figures (equal angle projection) of the upper and lower hemisphere, representing the orientation of garnet XA-GO-1E_II in the sample reference frame during OM- and SEM imaging and EBSD analysis. Garnet $< 111 >_{Grt}$ directions are labelled by the corresponding rutile needle SPO direction using the same colour as for the SPO frequency statistics. Additionally {110} normals of garnet facets are labelled (F1-F9), numbered as in Fig.: 14.
b) $\{110\}_{Grt}$ facet model generated in software *Vesta*, with original crystal orientation in the thin section reference frame. Black labels indicate facets facing towards the lower hemisphere, and white labels indicate facets facing towards the upper hemisphere. The thin section cut-plane $(205)_{Grt}$ on the right reveals the traces of those facets.

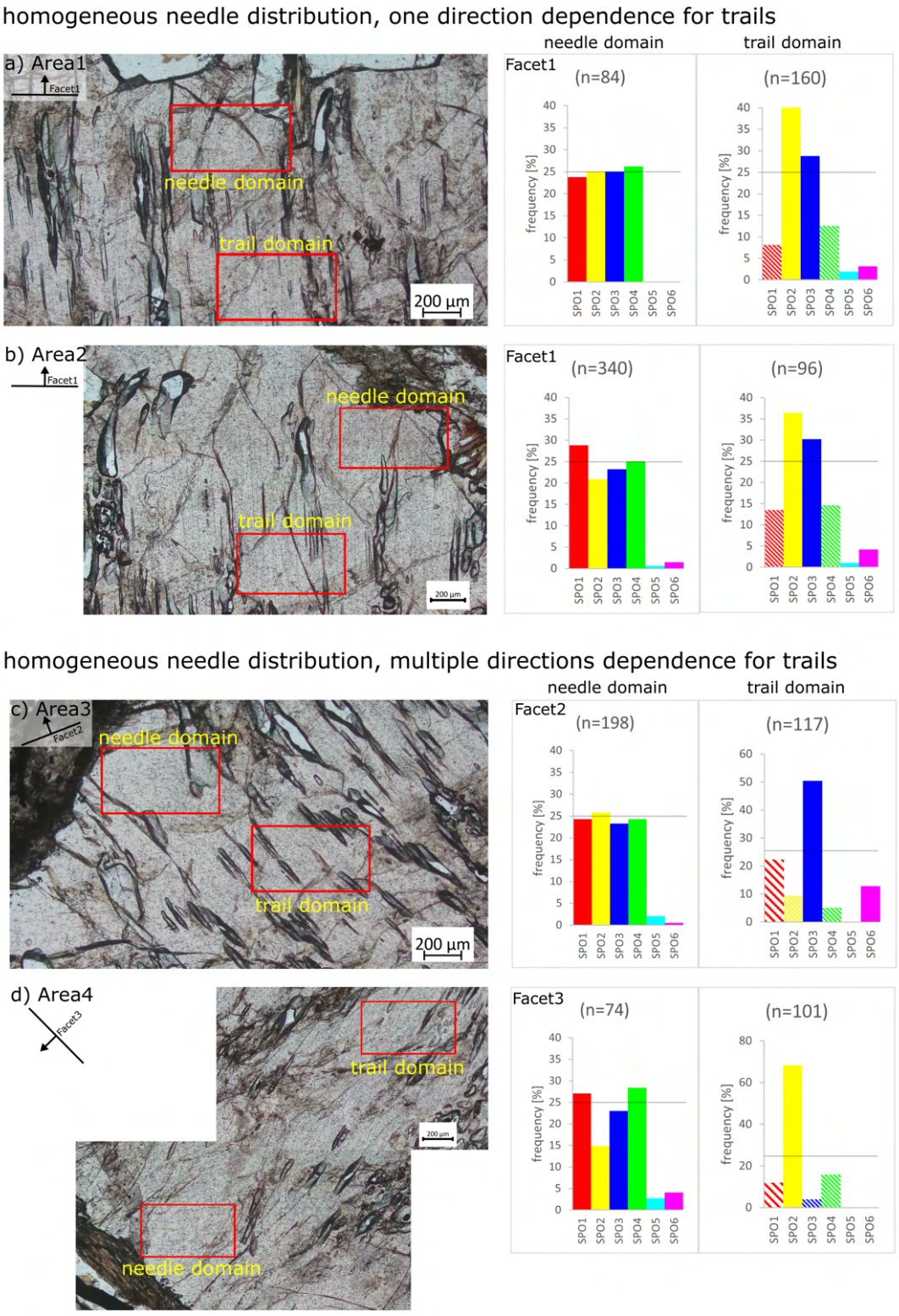
homogeneous needle distribution, one direction dependence for trails
needle domain
trail domain
a) Area1
Facet1
needle domain
trail domain
200 µm
Facet1
(n=84)
(n=160)
frequency [%]
SPO1 SPO2 SPO3 SPO4 SPO5 SPO6
b) Area2
Facet1
needle domain
trail domain
200 µm
Facet1
(n=340)
(n=96)
homogeneous needle distribution, multiple directions dependence for trails
needle domain
trail domain
c) Area3
Facet2
needle domain
trail domain
200 µm
Facet2
(n=198)
(n=117)
d) Area4
Facet3
trail domain
needle domain
Facet3
(n=74)
(n=101)

Figure 16.

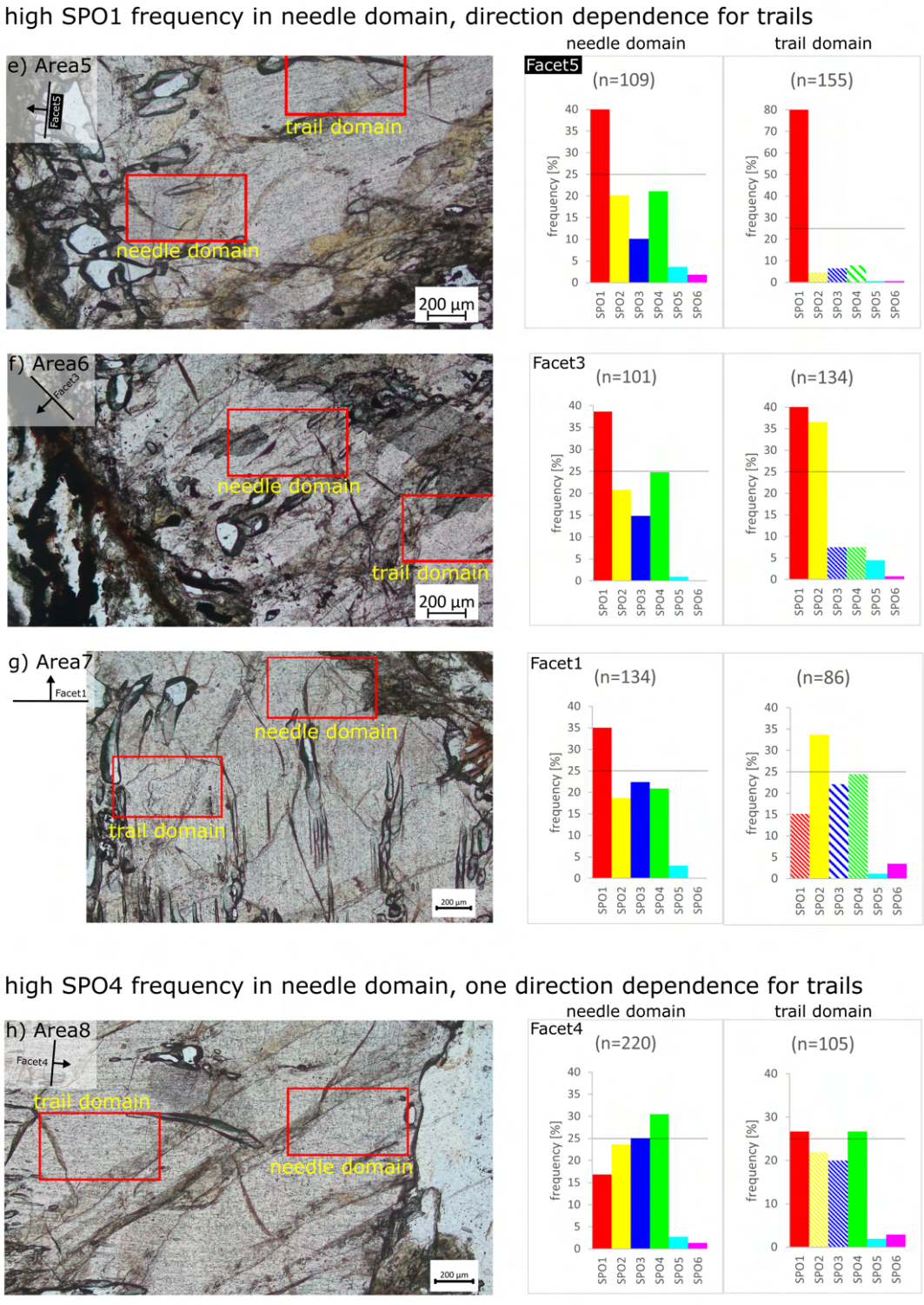
high SPO1 frequency in needle domain, direction dependence for trails
needle domain
trail domain
e) Area5
Facet5
trail domain
needle domain
200 µm
Facet5
(n=109)
(n=155)
f) Area6
Facet3
needle domain
trail domain
200 µm
Facet3
(n=101)
(n=134)
g) Area7
Facet1
needle domain
trail domain
200 µm
Facet1
(n=134)
(n=86)
frequency [%]
SPO1
SPO2
SPO3
SPO4
SPO5
SPO6
high SPO4 frequency in needle domain, one direction dependence for trails
h) Area8
Facet4
trail domain
needle domain
200 µm
Facet4
(n=220)
(n=105)

Figure 17.

to depend on multiple facet directions. This conclusion is consistent with the results of SPO frequency statistics of Area4 (Fig.: 16 d)), where the main garnet growth- and inclusion trail direction is determined by facet3 (lower hemisphere), to which SPO3 & SPO4 are parallel. The neighbouring growth sector of facet8 restricts the development of SPO1 & SPO4, resulting in the favoured frequency of SPO2 in the trail domain of Area4.

The other areas on page 35 show SPO frequencies that deviate from the general observation described above regarding the needle domain. In Areas 5, 6 and 7 (figures 17 e), f), g), respectively), the SPO frequency statistics for the needle domain show high SPO1 frequencies. The trail domain of Area5 is located in garnet growth sector associated with facet5 (upper hemisphere) in close proximity to facet3 (lower hemisphere). The trail domain of Area6 is located within the garnet growth sector of facet3. The SPO frequency distributions for both areas follow the dependence of an $< 110 >_{Grt}$ direction: SPO1 & SPO2 are oriented at 35°angle with respect to the growth direction the garnet sector associated with facet3. These two SPOs are dominant in Area6. In Area5, due to its close proximity to sector boundaries, and due to observed trail directions along multiple $< 112 >_{Grt}$, the resulting observation is the prevalence of SPO1. The SPO frequencies in this area are possibly influenced by multiple growth directions.
Of particular note are the needle domains in Area5 and Area6, which both also have a high prevalence of SPO1.
Area7 also displays this some preference for SPO1 in the needle domain, but the frequencies of other $< 111 >_{Grt}$ SPO are distributed more evenly. In the trail domain, the growth sector associated with facet1 controls the trail directions, thus enabling the development of SPO2 and SPO3. Additionally, while a subordinate $< 112 >_{Grt}$ trail direction is present, the abundance of rutile needles with a high aspect ratio suggests, that this selected area represents the transition of a trail domain to a needle domain. Therefore, the SPO frequencies of this area should be regarded with caution.
In Area8 (Fig.: 17 h)) the SPO distributions do not conform to any previously described pattern. The growth direction of the growth sector associated with facet4 is difficult to discern from the SPO frequency statistics of the trail domain. The observed trails show multiple, even crosscutting directions, aligning with the $< 110 >_{Grt}$ of facet4, a $< 112 >_{Grt}$ or another undefined direction. Rutile crystals with SPO1 and SPO4, which are slightly more frequent than 25°, seem to be preferred by the growth direction of the $\{110\}_{Grt}$ sector. In the needle domain, SPO4 is the most dominant and SPO1 is the least dominant $< 111 >_{Grt}$ SPO, which both are unusual observations.

The SPO frequencies are only gained from optical microscopy. This bears an error by the thin section's cutting effect, as well as an uncertainty due to the potential proximity of some areas to neighbouring growth sectors that are located above or below the thin section plane. Those errors were not considered in the SPO frequency statistics.

4.5. Crystallographic oriented relationships

By filtering all EBSD crystal orientation data of 518 rutile crystals, of various shapes and sizes, the rutile crystals were assigned to defined COR groups (Griffiths et al., 2020), according to their crystallographic orientation relationship with the host garnet lattice. All restrictions and angular thresholds of the COR groups are listed in appendix A.3 and A.4. The classification routine, according to Griffiths et al. (2020), determined crystallographic correlation between rutile inclusions and the garnet host, to which 90.3% of all single rutile crystals pertained. Of all rutile inclusions, 64.5% pertain to the COR group RA, which is characterised by the directional relationship $< 103 >_{Rt}$ parallel to the $\{111\}_{Grt}$ plane normal. This relationship bears a degree of freedom for the other crystallographic directions of rutile. In this case the $< 001 >_{Rt}$ directions, as described in Proyer et al. (2013), align in a cone-like arrangement around the $\{111\}_{Grt}$.
Consequently the rutiles' a-axes lie in $\{111\}_{Grt}$ planes. So far this result resembles the COR statistics from EBSD crystal orientation data observed by Proyer et al. (2013). Even when comparing the COR frequencies of the Proyer et al. (2013) data (n=213), in which *"rutile needles enclosed in the outer zone of a single garnet crystal"* were studied, with the newly acquired data (n=518) from the Xanthi sample, the distribution of single rutile inclusions in COR groups is similar, despite the increased data size in the current study, and the extension of the investigations to the inclusion trails (see Fig.: 19). Focusing to the rutile needles (n=227), defined by Type-4 intergrowths in the needle domain (Grt2c), increases the rate of success of the COR classification script to 98.2%. The elongation direction of the rutile needles corresponds to a $< 103 >_{Rt}$ direction (Fig.: 18), or in other words, the rutile inclusions are elongated perpendicular to the $\{405\}_{Rt}$ plane. The correlation of $< 103 >_{Rt}$ parallel to $\{111\}_{Grt}$ (RA group, angle threshold = 2°) is found for 92.4% of the needles. Therefore the rutile needles from a shape oriented relationship (SOR) with the garnet host lattice.
On the other hand, for trail inclusions (n=178), which are defined as Type-3 inclusions in the trail domain (Grt2b), there is already a higher percentage of single rutile crystals that cannot be correlated to any known COR group (n=30). The measured trail inclusions pertain for 83.1% to axial relationships with the garnet host lattice and only for 64.4% to specific crystallographic orientation relationships with said host. Those rutile crystals in the trail domain, that can be categorised into COR groups are associated with various axial relationships with the garnet host crystal, as shown by the COR classification results in the histogram of figure 19 a). Despite this, RA group still makes up 45.3% of the trail inclusions. The higher frequency of other COR groups compared to the data from needle domains suggests a wider range of possible axial relationships between the host and the inclusions in trail domains. There, the axial relations RB and RC each constitute 10.7%
Therefore, the differences in the inclusion's microstructure do affect the axial relationship classification: needle inclusions (n=227) are primarily found in one specific COR group (RA), while trail inclusions (n=178), which also appear in this group, are found in a variety of COR groups. Additionally, neither for needle nor trail inclusions the axial relationship $< 001 >_{Rt} \parallel \{100\}_{Grt} < 5°$ (RJ-group) was found.

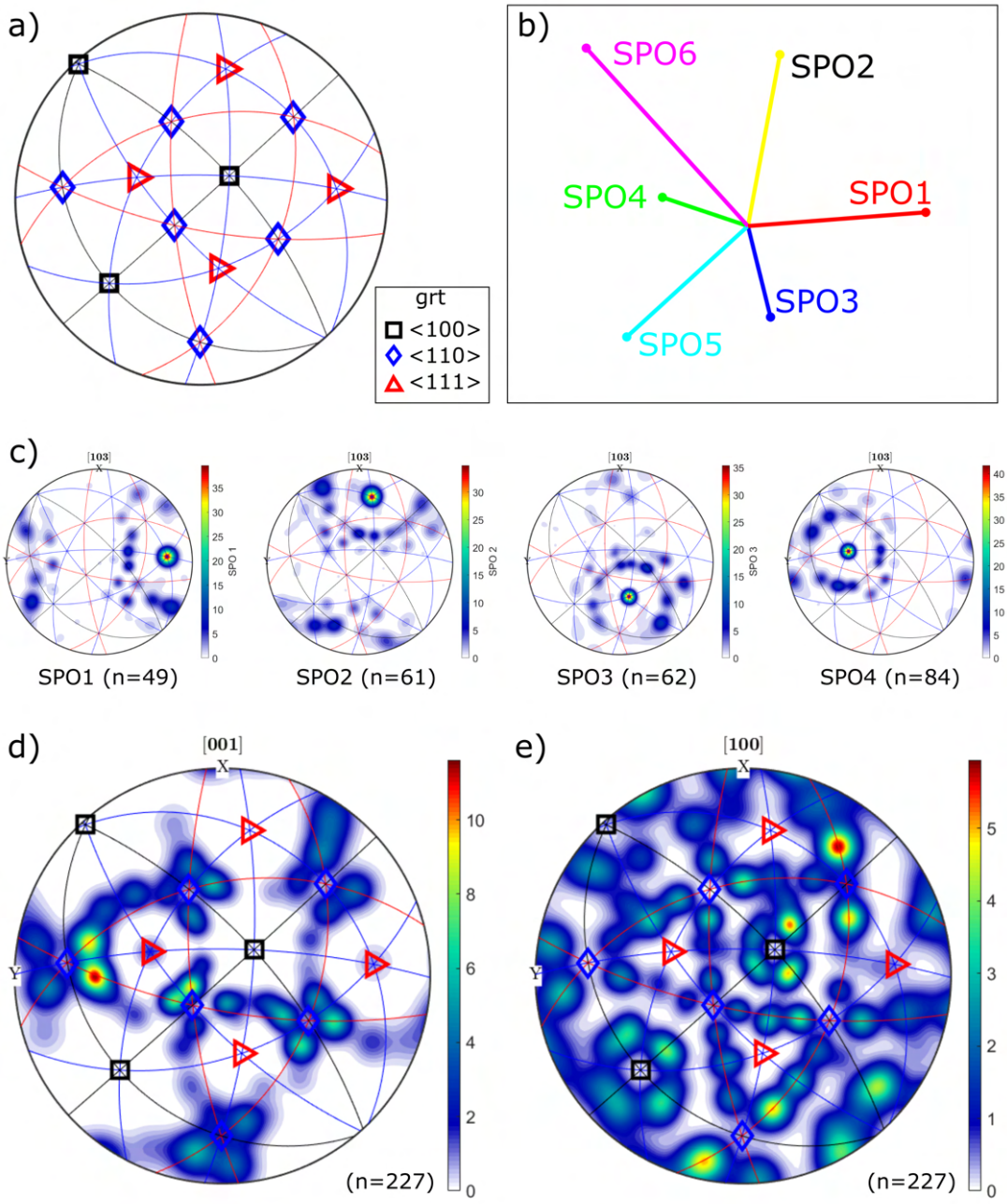

Figure 18.: All Pole figure are equal angle, upper hemisphere projection showing the mean garnet orientation in sample reference frame. a) directions and great circles in garnet. b) Projection of rutile needle SPO1-6 onto the thin section surface, as observed in OM, and correlated to the corresponding crystal direction of garnet, derived from EBSD analysis. c) Orientation data was filtered only by SPO direction as observed in OM (all domains). Resulting in density plots (Half-width 5°), which each has a $< 103 >_{Rt}$ density maximum at the specific $< 111 >_{Grt}$, that corresponds to their SPO direction. Orientation data, filtered for needle inclusions (all SPOs & needle domain), showing orientation density in d) $< 001 >_{Rt}$ and e) $< 100 >_{Rt}$. The former cluster in a "cone-like" arrangement around $< 111 >_{Grt}$, the latter align to $\{111\}_{Grt}$.

Rutile inclusions that occur as polymineralic inclusions in association with kyanite, quartz, or Zn-spinel do not seem to have any particular axial relationship with the garnet host. They pertain to COR groups with similar frequencies of all other rutile inclusions studied. Also the COR classification results for twinned rutile crystals do not differ from the general trend. However, two axial relations are found for each single rutile inclusion (Fig.: 13). The COR classification returns dominantly RA-group (90%) for the twinned rutile crystals, each paired with an other axial relationship, depending on the twin law (e.g.: RA $\leftrightarrow$ RG).

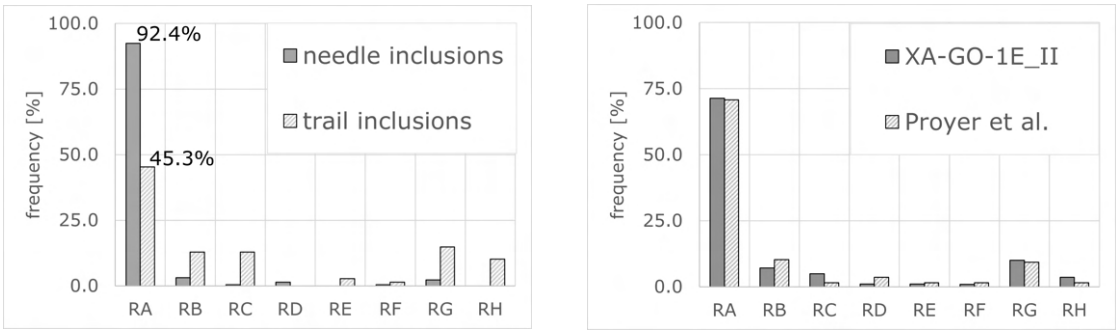

Figure 19.: left) COR-groups histogram of data sets filtered by microstructure. Needle inclusions in needle domain (n=223) correlate strongly to RA group, with a specific axial relation. Equant inclusions in trail domain (n=148) vary more. All COR groups, and their defining axial relations are listed in appendix A.3. right) Comparison of average Xanthi data set (XA-GO-1E_II, n=468) with Proyer et al. (2013) data set (n=195), both with identical classification routine. The frequencies of COR groups are pretty similar.

5. Discussion

5.1. Pressure and temperature estimation

The estimated temperatures calculated from RSCM for graphite, enclosed in both garnet and rock matrix, yielded $T = 510°C \pm 50°C$. This temperature is also expected for the dynamic recrystallization (bulging/SGR) of quartz in the matrix. Thermometry based on RSCM only records the last temperature, which generates the evident carbon order. These data tend to bear a uncertainty influenced by heterogeneities within the sample ($\pm 50°$, Beyssac et al. (2002)). This temperature range resembles the last thermal overprint of the rock. For the geological unit of the studied sample, still higher temperatures were considered in other publications: Krenn et al. (2008), "D2 shearing stage": $700°C$; Proyer et al. (2013): $850° \pm 50°C$. As no other thermometer, apart from RSCM, was uzilised in this study, these higher temperatures can neither be confirmed nor disproved.
The estimated residual pressures gained from RSQI range from 0.13/0.18 GPa to 0.25 GPa for quartz inclusions in garnet (Grt1/Grt2), and 0.4 to 0.5 GPa for quartz inclusions in kyanite. Once the maximum pressure values are applied to *EosFit-Pinc* (Angel et al., 2017b), at ambient 22°C, the resulting trends of the isomeke, calculated from the entrapment relation between inclusion and host, are plotted in figure 20. The isomekes are consistent with both the estimation by Krenn et al. (2008), considering P/T peak conditions of $1.3\,GPa$ at $700°C$, and the estimation by Proyer et al. (2013) yielding $1.1 - 1.6\,GPa$ at $850° \; C \pm 50°C$. Both conditions of peak metamorphism in the temperature range between $T = 700 - 900°C$ align with the isomekes. Only the peak pressures of Mposkos and Krohe (2000) conflict with the result of the *EosFit-Pinc* approach. It is important to note, that the reported P/T paths in the literature suggest, that the period of garnet growth only reflects decompression stages of metamorphism stages, whereas growth of garnet in metapelites is considered to occur due to dehydration reactions, usually associated with heating and/or burial.
Another evidence of high temperature conditions overprinting the Grt2 growth stage is shown in figure 12: the intragranular misorientation of 2° results from deformation that affected the entire garnet crystal. Low angle grain boundaries in garnet seem to have migrated through the garnet crystal on a macroscopic scale. The rutile inclusion obviously pinned the migrating low angle boundary. Dynamic recrystallisation of garnet is supposed to require high temperature conditions and a sufficient strain force (Ji, 1998; Prior et al., 2000; Bestmann et al., 2008).

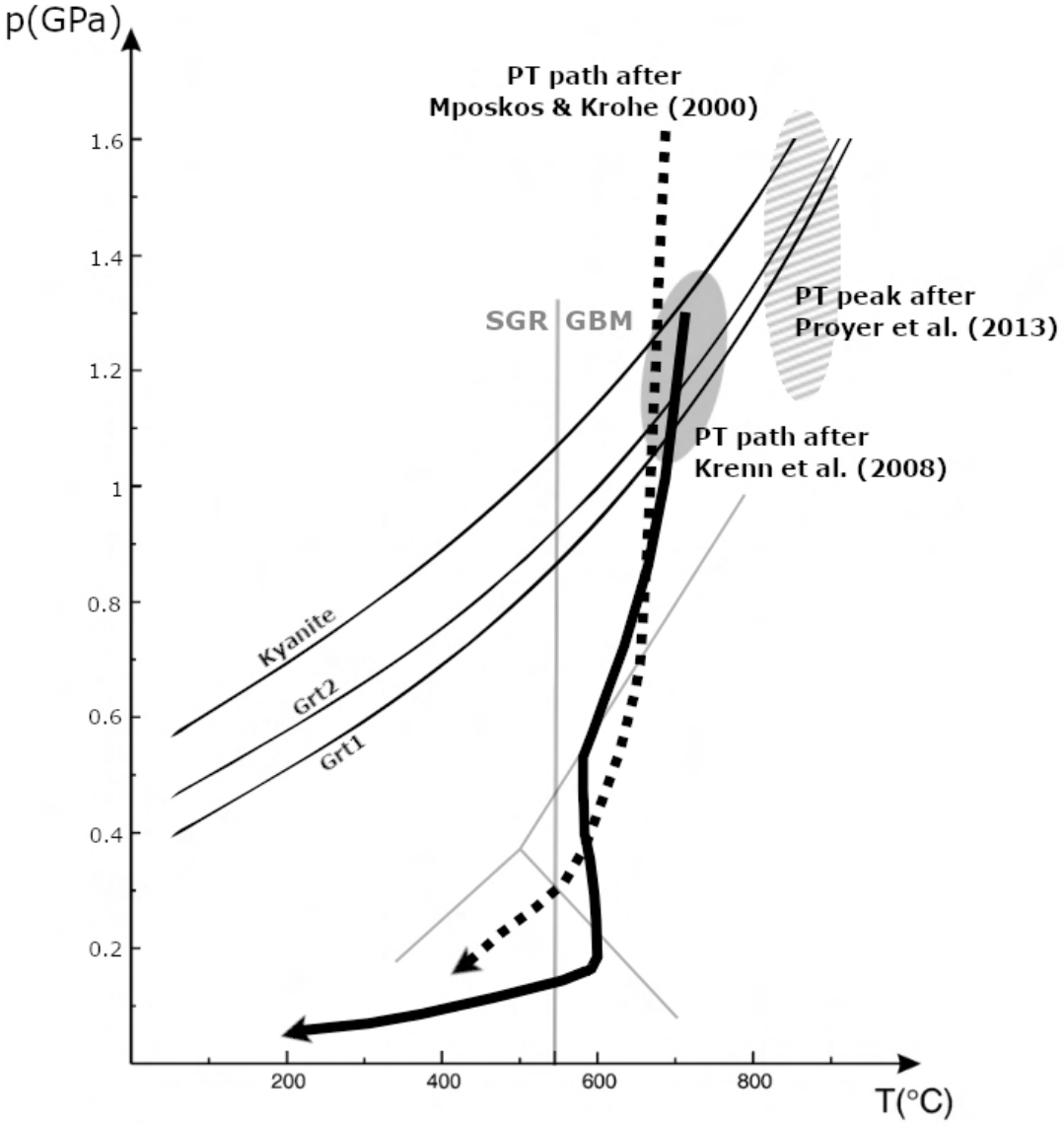

Figure 20.: The P/T diagram illustrates the estimated retrograde path (dashed line) of Mposkos and Krohe (2000), the more refined path (solid black line) of Krenn et al. (2008), with their estimated P/T peak marked in grey and the P/T range of Proyer et al. (2013), with hatched marking. The three isomekes from Grt1/Grt2/Kyanite, calculated with software *EosFit-Pinc*, align with the P/T estimation of Krenn et al. (2008), as well as with the higher P/T conditions of Proyer et al. (2013). Additionally, the transitions of the Al_2SiO_5 polymorphs and subgrain rotation/grain boundary migration of quartz are also shown (figure modified after Krenn et al. (2008)).

5.2. Correlation of CORs and SPOs

The results of COR classification indicate that the axial relationships between garnet and rutile vary based on the habit of the inclusion and the microstructural domain. Particular differences in COR characteristics were observed between needle-shaped rutile inclusions in the needle domain of garnet (Grt2c) and equant rutile inclusions in the trail domain (Grt2b).
Almost all (92.8%) needle-shaped rutile crystals have a definite axial relation with the garnet host, namely pertaining to the RA group: one of $< 103 >_{Rt}$ parallel to one of $\{111\}_{Grt} < 2°$. In addition, their crystal shape shows the needle elongation parallel to the corresponding $< 111 >_{Grt}$. Therefore, the crystallographic and shape preferred orientation of needle-shaped inclusions are linked, and both are clearly controlled by the garnet host lattice. According to results from SPO frequency counting, no certain prevalence for any particular $< 111 >_{Grt}$ was found in 50% of the studied Grt2c areas. There, the shape preferred orientations of rutile needles are distributed equally between the four equivalent $< 111 >_{Grt}$ directions (Fig.: 16). Three areas of Grt2c deviate from this trend, as rutile needle SPOs favour particular $< 111 >_{Grt}$ direction. It seems that those directions are preferred, which are subparallel to the earliest foliation plane (SPO1 and SPO4), which had been overgrown and enclosed by garnet. Area5 and Area6, in figure 17, are placed in proximity to a garnet domain that hosts numerous Type-1 inclusions of quartz and graphite, which reflect the Grt1 foliation and the deformation shadow (Grt2a). Therefore, it is hypothised, that the preexisting foliation may represent a heterogenity that affects SPO developement of rutile needles. As the 3D orientation of the foliation plane was not obtained from the particuar thin section used for SPO and COR investigation this hypothesis is based only on the orientation of the trace of the foliation plane observed in the thin section.
The inclusions without any SOR with the garnet lattice defining the trail domain in garnet (equants in Grt2b) return a different distribution of the COR groups comparing to the needle inclusions in Grt2c. Equant rutile crystals forming inclusion trails comprise a significantly lower fraction that can be categorised into an axial relationship. Furthermore, the equant trail inclusions show a higher variability in COR types. Although the RA group is still favoured with 37.6%, other axial relations were frequently observed, as for example the COR groups RB and RC, which correlate the a- and c-axes of rutile to the garnet growth facets $\{110\}_{Grt}$ and $\{112\}_{Grt}$. These two COR groups amount to 21.4% of the equant trail inclusions. This applies to the results of the SPO frequency count. Whereas rutile needles with low aspect ratio might influence the SPO frequencies of the trail domain, there is a clear dependence of the shape preferred orientation on the garnet growth facets, as reflected by the SPO distribution regarding the different equivalent garnet $< 111 >_{Grt}$ directions. It seems that only those rutile crystals, nucleated with particular crystallographic axial relationship (pertaining to RA group), can develop a needle shape, whereas others remain of equant shape. The trail inclusions pertaining to the COR groups RB and RC are correlated to growth facets of the garnet host. Furthermore, a high fraction of rutile crystals that constitute the trails could not be

assigned to any known COR. Therefore, the trail inclusions derive their crystallographic and shape characteristics from interaction with the garnet growth facet, or crystallise without remarkable influence by the hosting garnet lattice.

5.3. Scenarios of origin of rutile inclusions in garnet

5.3.1. Needle-shaped rutile inclusions

In the needle domain of garnet (Grt2c), 98.2% of the needle shapes rutile crystals, with high aspect ratio, show a COR with garnet according to classification by Griffiths et al. (2020). These rutile crystals show a dominant axial relationship to the garnet host (RA group) and constitute a 3D framework by their associated shape preferred orientation throughout the whole garnet single crystal. These results indicate that the needle-shape rutile crystals nucleated within the pre-existing host lattice. The axial relation $< 103 >_{Rt} \parallel \{111\}_{Grt} < 2°$ seems to be an energetically favourable orientation of the nuclei, which further allows the inclusions to preferably grow along the particular $< 103 >_{Rt}$ that is parallel to a $< 111 >_{Grt}$. Especially as the SPO directions of these rutile needles are evenly distributed between the 4 equivalent $< 111 >_{Grt}$ directions, a scenario of rutile precipitation within garnet (like exsolution or open system precipitation) seems to be the most likely origin of the rutile inclusions. The low frequency of rutile needles with an SPO along $\{100\}_{Grt}$, which are restricted to needles with low aspect ratio, supports this scenario. It seems unlikely, that inclusions from an precipitation origin form in a less favourable energetic orientation. Additionally, rutile needles were observed in an even lower frequency with a shape preferred orientation, which neither could be correlated to any $< 111 >_{Grt}$ nor any $< 100 >_{Grt}$. This observation further supports the precipitation scenario.
The abundance of rutile needles throughout the whole garnet supports an inclusion origin by intragranular precipitation in garnet, namely by nucleation of rutile in an energetically favourable orientation, and the development of needles in the framework of the host lattice.

As discussed by Hwang et al. (2007b) and Proyer et al. (2013) the source of Ti is questionable. For garnet, the solution of Ti depends on temperature. With the estimated peak temperature of the Ky-Grt geniss from Xanthi in mind, the solubility should reach circa 0.072 Ti atoms per formula unit (apfu) ($P = 1.5\,GPa$, $T = 1200°C$), as proposed by Kawasaki and Motoyoshi (2016). However, the high abundance of observed rutile needles raises questions about the possibility of exsolution of rutile from garnet in a closed intragranular system (Proyer et al., 2013). On the other hand, the presumed low mobility of Ti within garnet to diffuse into garnet from an external source also casts doubt on the idea of pure external mechanisms. The source of Ti to form the rutile precipitates in garnet therefore remains ambiguous.

5.3.2. Inclusions of the trail domain

Contrasting to the needle shaped inclusions with high aspect ratio, the origin of equant rutile inclusions in the trail domain of garnet (Grt2b) clearly cannot be explained by a mechanism of intragranular precipitation in garnet, as a high fraction (30%) of these rutile crystals does not have any crystallographic relationship with the garnet host lattice. The equant rutile inclusions constitute trails, which show a clear microstructural relationship with the corresponding host growth facet, mainly representing $\{110\}_{Grt}$ and subsidiary $\{112\}_{Grt}$ crystal planes. The COR groups RB and RC (each constituting 10.7% of the trail inclusions) also correlate to axial relations of rutile to facet planes. Thus, a co-growth scenario is suggested for the trail inclusions, involving the nucleation or attachment of rutile at a facet of garnet, followed by subsequent overgrowth and enclosure by garnet. This scenario is confirmed by all areas, where SPO frequencies of rutile needles differ between those $< 111 >_{Grt}$ directions lying parallel to the growth facet and those lying at a high angle with respect to the garnet growth facet. For example, the SPO frequencies in Area1 and Area2 (Fig.: 16) show evidence for facet dependence, as two SPOs, which are associated with $< 111 >_{Grt}$ at a 35° angle to the specific $< 110 >_{Grt}$ facet yield a significantly high frequency than the other two SPO directions that are lying in the $\{110\}_{Grt}$ facet plane. For Area3 and Area4 (Fig.: 16), the position of these areas close to a sector boundary seems to indicate an effect of the neighbouring $\{110\}_{Grt}$ facet on the SPO frequencies. It is hypothesised, that a (certain) micro step surface of garnet was established during garnet growth. Such a micro step surface is schematically displayed in figure 21, where multiple local $\{110\}_{Grt}$ and $\{112\}_{Grt}$ facet segments result in development of a main $\{110\}_{Grt}$ facet. These short local segments of a stepped growth facet could cause deviating trends of the inclusion trails within a single garnet growth sector. Also, both the micro-CT model and facet models, gained from crystal orientation data, show the primary garnet habit is constituted by predominantly $\{110\}_{Grt}$ facets, whereas the "rounded" corners could reflect subordinate $\{112\}_{Grt}$ facets.

An overgrowth scenario posts the (Type-3) inclusions are potential remnants of the matrix, which are incorporated during a phase of rapid growth of the garnet host crystal (Andersen, 1984; Keller and Ague, 2019). This hypothesis is challenged by the question why only rutile is found to develop inclusion trails, whereas the other matrix phases do not. Type-3 inclusions are expected to be phases that are in chemical equilibrium with the rock matrix. The lack of other inclusion phases requires an epitaxial nucleation of rutile crystals on the garnet surface during its growth, which separates the rutile crystals from other matrix phases. This type of nucleation may be demonstrated in the axial relation RA, which make up to 37.6% of the trail inclusions in the COR classification. As for the needle domain, this COR seems to be the most energetically favourable orientation. This is shown by in rutile needles with low aspect ratio in the trail domain of garnet. Many of these inclusions originate at sites along the said trails. Therefrom, they developed their elongation direction according to the prescribed axial relationship with garnet.

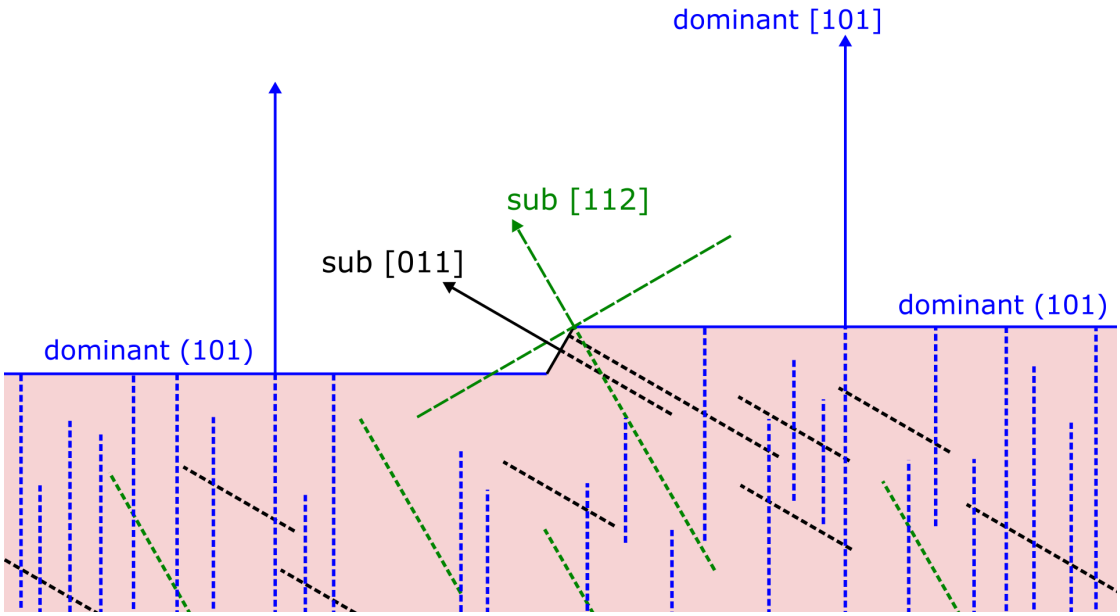

Figure 21.: Schematic sketch of a section perpendicular to the dominant $(101)_{Grt}$ facet (blue) with the $< \bar{1}\bar{1}1 >_{Grt}$ direction as viewing direction. The combination with $(011)_{Grt}$ micro steps (black) yield an $(112)_{Grt}$ trend (green). The growth direction of each facet is indicated by an arrow. Inclusion trails form perpendicular to the facet planes of garnet, when rutile crystals are incorporated in garnet by an attachment and overgrowth scenario.

Other scenarios supported by Hwang et al. (2007a) or Griffiths et al. (2014) state, that equant trail inclusions originate along micro cleavages or micro cracks during decompression. The former may result in trail directions along $\{110\}_{Grt}$ and $\{112\}_{Grt}$ but does not explain the restriction of the trails to its domain. The latter might apply for trails, which are not correlated with particular growth directions of garnet. Hwang et al. (2019) further invested the origin of rutile inclusions by exsolution along microcracks. In the studied material, candidates for by-products of potential rutile precipitation from Ti-bearing garnet are apatite and gahnite, which were observed in polymineralic inclusions with rutile. Apatite was only found once in the trail domain and was associated with an equant rutile. Zn-spinel (gahnite) was discovered in every domain studied and was correlated with both needles and equants. However, Hwang et al. (2019) state the precipitation of rutile in association with spinel by garnet decomposition must balance with pyroxene as an additional precipitation product.

5.4. Utilising large EBSD data sets

While large EBSD data sets, help to identify and quantify multiple crystallographic orientation relationships between inclusions and their host crystal, the ability of COR characteristics to trace particular inclusion origins is still a matter of discussion. Comparison of the new EBSD data set with the data from the same rock type and locality by Proyer et al. (2013) clearly show indisputable similarities in the COR frequencies, despite of different garnet crystals were analysed, applying different instrumental parameters, years apart. The Proyer et al. (2013) data set resembles the average COR distribution of the entire new data set, when merging all data from both the trail and the needle domains of garnet (Fig.: 19). When filtering the current data set for particular microstructural domains of garnet or a particular crystal shape of rutile, the COR data deviates strongly from the average distribution. Thus, the statistics of the crystal orientation data are strongly affected by the selection of particular studied inclusions and host domains. Keller and Ague (2019) expressed the wish for comparability between data sets and the development of "fingerprints" based on particular host-inclusion relationships. When uniformly applied, these should point to certain formation mechanisms of the host-inclusion system. According to the results of this study, the details of the COR characteristics greatly depend on the particular microstructure of the inclusions.
Another EBSD data set was reported by Keller and Ague (2019), who studied multiple inclusion phases in metapelitic garnet. Rutile with a clear $< 111 >_{Grt}$ SPO (n=69) and the garnet host showed COR characteristics that clearly deviate from those of the current study. Rutile inclusions reported by Keller and Ague (2019) were 57.4% RA group, while the other groups all constituted less than 10% of their data set. Most of the the rutile crystals were classified as part of COR2 or COR3 (named after Hwang et al. (2015), see appendix A.3), each at approximately 24%. The data from the Xanthi metapelite returns only COR2 (with 55.6%) as the main crystallographic orientation relationship for rutile crystals with clear $< 111 >_{Grt}$ SPO. In conclusion, the two data sets of samples from different metapelitic rocks exhibit differing frequencies of specific CORs, but both data sets show a similar trend of the predominant axial relationship between rutile and garnet, being $< 103 >_{Rt} \parallel \{111\}_{Grt} < 2°$.
Comparison of data from the current study with those from samples of different origin yielded even further differences. Griffiths et al. (2020) studied metapegmatite garnet, which showed concentric and sector zoning, as well as deviating COR characteristics in different garnet domains. Over all, the entire rutile data set (n=165), run through the same *mTex* script, results in the major axial relation RD: $< 001 >_{Rt} \parallel \{111\}_{Grt} < 5.5°$ for 82.4% of all measured rutile crystals. The COR characteristics of highly different rock type seem to strongly deviate when comparing sample from metasedimentary and magmatic rocks. The application of COR characteristics for "fingerprinting" therefore seems to be conceivable, at least for distinction between rocks of different origin.

6. Conclusion

Macroscopic observations on garnet

Garnets from the Xanthi location exhibit three concentric growth zones, identified as Grt1, Grt2 and Grt3, based on inclusion microstructure. These zones comprise different generations of inclusions with possibly different origin. Grt1 represents the garnet core grown over and enclosing quartz, rutile and graphite, which show a shape preferred orientation (SPO) correlated to a foliation that has formed prior garnet crystallisation. Grt2 displays sector zoning based on inclusion fabrics, consistent with reports of other poikiloblastic garnets and is further subdivided in a "trail domain" and a "needle domain". Grt3 represents the outermost rim of garnet, that is largely free of inclusions. A string of inclusions, consisting of graphite, rutile, or mica, represents an external foliation, which was overgrown by Grt3.

Studies on the habit of garnet, performed by micro-CT and facet models, based on crystal orientation data, indicate the garnets in the studied sample form growth pyramids, resulting in macroscopic $\{110\}_{Grt}$ facets. At junctions, "rounded" corners possibly represent subordinate $\{112\}_{Grt}$ facets.

Microstructure and texture of rutile inclusions in garnet

Rutile needles within the entire garnet host show elongation with a distinct SPO that correlates predominantly with the $< 111 >_{Grt}$ directions, thus reflecting a shape orientation relationship (SOR). Furthermore, the predominant part of rutile inclusions pertain to a crystallographic orientation relationship (COR) with the garnet host lattice. Still, significant differences in the relative frequencies of rutile crystals with particular COR were observed when comparing microstructurally different sets of rutile crystals, or rutile inclusions in different domains of garnet.
In the needle domain of garnet, 92.4% of rutile needle inclusions with high aspect ratio and SPO $\parallel \{111\}_{Grt}$ are classified as members of the RA-group, defined by the axial relationship $< 103 >_{Rt} \parallel \{111\}_{Grt} < 2°$.
Statistics of SPO frequencies, gained from OM images in the needle domain, reveal an equal distribution of rutile inclusions among the four crystallographic equivalent SPO directions $\parallel \{111\}_{Grt}$.

Contrastingly rutile inclusions in the trail domain of garnet, occur as needles with low aspect ratio or as equidimensional inclusions (equants) that are arranged along (curvi)linear inclusion trails. These trails correlate with $< 110 >_{Grt}$ or $< 112 >_{Grt}$ of the garnet host. One of these trail directions usually is the most common in a particular growth sector of garnet, namely the trail direction orthogonal to the particular corresponding facet plane of garnet. The COR-classification of equant rutile crystals yields a higher range of axial relationships compared to the needle inclusions.
Statistical analysis of SPO frequencies of non-equidimensional rutile inclusions in the trail domain shows a predominance of inclusions with SPO aligned along a high angle to the facet associated with a particular growth sector of garnet. Rutile inclusions with SPO parallel to said facet occur only at low frequency.

Mechanisms & scenarios of formation of rutile inclusions

The microstructural and textural differences between the needle and trail domains of garnet imply distinct origins of the associated inclusions. The textural and microstructural characteristics of rutile inclusions in the trail domain point to an attachment and overgrowth mechanism of inclusion formation, which is syngenetic with garnet growth. During this process, rutile crystals nucleate at, or attach to the garnet growth interface, which is constrained by the micro-/nanotopography of garnet facet planes.
In contrast, the needle inclusions are inferred to have formed through an intragranular precipitation mechanism that postdates garnet growth. Thus, only energetically favourable sites along the lattice of garnet, and orientations of the rutile crystals are expected to form, without any preference regarding the facet plane of garnet. This is reflected by both the distinct SOR and the strict COR of needle-shaped rutile with the garnet host lattice.

Methods & Outlook

The available SPO data of rutile inclusions in garnets from two different samples of metapelitic Ky-Grt-Gneiss from locality Xianthi (Greece) clearly confirm the consistent SOR of rutile needles with the garnet host lattice, parallel to $< 111 >_{Grt}$. For the studied lithology of the Kimi Complex, models of the garnet orientations now can be constructed from the trace of the four predominant SPO directions of needle-shaped rutile inclusions, as derived from optical microscopy.

Statistical analysis of SPO frequencies, applied to garnet of dodecahedral habit for the first time, yielded useful information on the relative timing of crystallisation of garnet host and rutile inclusions. However, the gained frequencies strongly vary even in the same garnet domain when considering particular inclusion habits

and arrangements. Polmineralic inclusions, as well as garnet domains close to sector boundaries or sites affected by overprinting of the host-inclusion system must be avoided, in order to obtain unambigous results. Selection of representative areas for the statistical analysis of SPO frequencies profit from careful and proper preparatory study based on combined optical microscopy, micro-CT analysis and host crystal facet orientation modelling.

Similar to the analysis of SPO frequencies, the COR classification of rutile inclusions and the garnet host based on EBSD orientation data, shows a strong interrelation with the particular inclusion microstructure. This study serves as a key example of correlated microstructure and texture analysis considering 3D geometries and arrangements. Linking microstructural properties with systematic investigation of crystallographic orientation data can provide crucial evidence of diverse formation scenarios of host-inclusions systems.
COR classification on a data set from Proyer et al. (2013), featuring a different specimen of the Xanthi Ky-Grt gneiss, yielded a comparable COR distribution pattern as the average COR classification of the new, much more comprehensive data set of this study. Still, the identified links between COR statistics and particular microstructural features of the rutile inclusions demand cautious selection of garnet host domains for correlated COR-SOR analysis. Altogether, this demonstrates the representativeness of this method and provides promising evidence, that the microstructure and texture of rutile inclusions in garnet host crystals can be used for fingerprinting.

Bibliography

I have made every effort to locate all owners of the image rights and have obtained their permission to use the images in this work. However, if you become aware of any copyright infringement, please contact me.

T. B. Andersen. Inclusion patterns in zoned garnets from Mager by, north Norway. *Mineralogical Magazine*, 48:21–26, 1984.

R. J. Angel, M. Alvaro, R. Miletich, and F. Nestola. A simple and generalised p–t–v eos for continuous phase transitions, implemented in eosfit and applied to quartz. *Contributions to Mineralogy and Petrology*, 172:1–15, 2017a.

R. J. Angel, M. L. Mazzucchelli, M. Alvaro, and F. Nestola. EosFit-Pinc: A simple GUI for host-inclusion elastic thermobarometry. *American Mineralogist*, 102(9):1957–1960, Sept. 2017b. ISSN 0003-004X. doi: 10.2138/am-2017-6190. URL `https://www.degruyter.com/document/doi/10.2138/am-2017-6190/html`.

R. J. Angel, M. Gilio, M. Mazzucchelli, and M. Alvaro. Garnet eos: a critical review and synthesis. *Contributions to Mineralogy and Petrology*, 177(5):54, 2022.

I. Arganda-Carreras, V. Kaynig, C. Rueden, K. W. Eliceiri, J. Schindelin, A. Cardona, and H. Sebastian Seung. Trainable Weka Segmentation: a machine learning tool for microscopy pixel classification. *Bioinformatics*, 33(15):2424–2426, Aug. 2017. ISSN 1367-4803. doi: 10.1093/bioinformatics/btx180. URL `https://doi.org/10.1093/bioinformatics/btx180`.

K. T. Ashley, M. Steele-MacInnis, and M. J. Caddick. QuIB Calc: A MATLAB® script for geobarometry based on Raman spectroscopy and elastic modeling of quartz inclusions in garnet. *Computers & Geosciences*, 66:155–157, May 2014. ISSN 0098-3004. doi: 10.1016/j.cageo.2014.01.005. URL `https://www.sciencedirect.com/science/article/pii/S0098300414000089`.

F. Bachmann, R. Hielscher, and H. Schaeben. Texture Analysis with MTEX – Free and Open Source Software Toolbox. *Solid State Phenomena*, 160:63–68, Feb. 2010. ISSN 1662-9779. doi: 10.4028/www.scientific.net/SSP.160.63. URL `https://www.scientific.net/SSP.160.63`.

M. Bestmann, G. Habler, F. Heidelbach, and M. Thöni. Dynamic recrystallization of garnet and related diffusion processes. *Journal of Structural Geology*, 30(6):777–790, June 2008. ISSN 01918141. doi: 10.1016/j.jsg.2008.02.007. URL `https://linkinghub.elsevier.com/retrieve/pii/S0191814108000321`.

O. Beyssac, B. Goffé, C. Chopin, and J. N. Rouzaud. Raman spectra of carbonaceous material in metasediments: a new geothermometer: RAMAN SPECTROSCOPY OF CARBONACEOUS MATERIAL. *Journal of Metamorphic Geology*, 20(9):859–871, Dec. 2002. ISSN 02634929, 15251314. doi: 10.1046/j.1525-1314.2002.00408.x. URL http://doi.wiley.com/10.1046/j.1525-1314.2002.00408.x.

V. Bosse, P. Boulvais, P. Gautier, M. Tiepolo, G. Ruffet, J. Devidal, Z. Cherneva, and I. Gerdjikov. Fluid-induced disturbance of the monazite Th–Pb chronometer: In situ dating and element mapping in pegmatites from the Rhodope (Greece, Bulgaria). *Chemical Geology*, 261:286–302, Apr. 2009. doi: 10.1016/j.chemgeo.2008.10.025.

D. Brown and R. A. Mason. An Occurrence of Sectored Birefringence Almandine from the Gagnon Terrane, Labrador. *The Canadian Mineralogist*, 32(pp):105–110, 1994.

K. W. Burton. Garnet-quartz intergrowths in graphitic pelites: the role of the fluid phase. *Mineralogical Magazine*, 50(358):611–620, Dec. 1986. ISSN 0026-461X, 1471-8022. doi: 10.1180/minmag.1986.050.358.06. URL https://www.cambridge.org/core/product/identifier/S0026461X0004055X/type/journal_article.

B. Cesare, F. Nestola, T. Johnson, E. Mugnaioli, G. Della Ventura, L. Peruzzo, O. Bartoli, C. Viti, and T. Erickson. Garnet, the archetypal cubic mineral, grows tetragonal. *Scientific Reports*, 9(1):14672, Oct. 2019. ISSN 2045-2322. doi: 10.1038/s41598-019-51214-9. URL https://www.nature.com/articles/s41598-019-51214-9. Number: 1 Publisher: Nature Publishing Group.

M. Enami, T. Nishiyama, and T. Mouri. Laser Raman microspectrometry of metamorphic quartz: A simple method for comparison of metamorphic pressures. *American Mineralogist - AMER MINERAL*, 92:1303–1315, Aug. 2007. doi: 10.2138/am.2007.2438.

T. A. Griffiths, G. Habler, D. Rhede, R. Wirth, F. Ram, and R. Abart. Localization of submicron inclusion re-equilibration at healed fractures in host garnet. *Contributions to Mineralogy and Petrology*, 168(6):1077, Nov. 2014. ISSN 1432-0967. doi: 10.1007/s00410-014-1077-4. URL https://doi.org/10.1007/s00410-014-1077-4.

T. A. Griffiths, G. Habler, and R. Abart. Crystallographic orientation relationships in host–inclusion systems: New insights from large EBSD data sets. *American Mineralogist*, 101(3):690–705, Mar. 2016. ISSN 0003-004X. doi: 10.2138/am-2016-5442. URL https://www.degruyter.com/document/doi/10.2138/am-2016-5442/html.

T. A. Griffiths, G. Habler, and R. Abart. Determining the origin of inclusions in garnet: Challenges and new diagnostic criteria. *American Journal of Science*, 320(9):753–789, Nov. 2020. ISSN 0002-9599, 1945-452X. doi: 10.2475/11.2020.01. URL http://www.ajsonline.org/lookup/doi/10.2475/11.2020.01.

M. J.-F. Guinel and M. G. Norton. The origin of asterism in almandine-pyrope garnets from Idaho. *Journal of Materials Science*, 41(3):719–725, Feb. 2006. ISSN 0022-2461,

1573-4803. doi: 10.1007/s10853-006-6500-4. URL http://link.springer.com/10.1007/s10853-006-6500-4.

G. Habler and T. Griffiths. Crystallographic orientation relationships. *European Mineralogical Union Notes in Mineralogy*, 16:541–585, 2017. ISSN 1417-2917. doi: 10.1180/EMU-notes.16.15.

R. J. Hemley. Pressure Dependence of Raman Spectra of SiO2 Polymorphs: alphaQuartz, Coesite, and Stishovite. In *High-Pressure Research in Mineral Physics: A Volume in Honor of Syun-iti Akimoto*, pages 347–359. American Geophysical Union (AGU), 1987. ISBN 978-1-118-66412-4. doi: 10.1029/GM039p0347. URL https://onlinelibrary.wiley.com/doi/abs/10.1029/GM039p0347. _eprint: https://onlinelibrary.wiley.com/doi/pdf/10.1029/GM039p0347.

S. L. Hwang, P. Shen, T. F. Yui, and H. T. Chu. TiO2 nanoparticle trails in garnet: implications of inclusion pressure-induced microcracks and spontaneous metamorphic-reaction healing during exhumation. *Journal of Metamorphic Geology*, 25(4):451–460, 2007a. ISSN 1525-1314. doi: 10.1111/j.1525-1314.2007.00705.x. URL https://onlinelibrary.wiley.com/doi/abs/10.1111/j.1525-1314.2007.00705.x. _eprint: https://onlinelibrary.wiley.com/doi/pdf/10.1111/j.1525-1314.2007.00705.x.

S. L. Hwang, T. F. Yui, H. T. Chu, P. Shen, H. P. Schertl, R. Y. Zhang, and J. G. Liou. On the origin of oriented rutile needles in garnet from UHP eclogites. *Journal of Metamorphic Geology*, 25(3):349–362, Mar. 2007b. ISSN 0263-4929, 1525-1314. doi: 10.1111/j.1525-1314.2007.00699.x. URL https://onlinelibrary.wiley.com/doi/10.1111/j.1525-1314.2007.00699.x.

S.-L. Hwang, P. Shen, H.-T. Chu, T.-F. Yui, and Y. Iizuka. Origin of rutile needles in star garnet and implications for interpretation of inclusion textures in ultrahigh-pressure metamorphic rocks. *Journal of Metamorphic Geology*, 33 (3):249–272, 2015. ISSN 1525-1314. doi: 10.1111/jmg.12119. URL https://onlinelibrary.wiley.com/doi/abs/10.1111/jmg.12119. _eprint: https://onlinelibrary.wiley.com/doi/pdf/10.1111/jmg.12119.

S.-L. Hwang, P. Shen, H.-T. Chu, and T.-F. Yui. On the forbidden and the optimum crystallographic variant of rutile in garnet. *Journal of Applied Crystallography*, 49 (6):1922–1940, Dec. 2016. ISSN 1600-5767. doi: 10.1107/S1600576716014151. URL http://scripts.iucr.org/cgi-bin/paper?S1600576716014151.

S.-L. Hwang, P. Shen, H.-T. Chu, T.-F. Yui, Y. Iizuka, and H.-P. Schertl. Rutile inclusions in garnet from a dissolution-reprecipitation mechanism. *Journal of Metamorphic Geology*, 37(8):1079–1098, 2019. ISSN 1525-1314. doi: 10.1111/jmg.12502. URL https://onlinelibrary.wiley.com/doi/abs/10.1111/jmg.12502. _eprint: https://onlinelibrary.wiley.com/doi/pdf/10.1111/jmg.12502.

Z. Ivanov, D. Dimov, S. Dobrev, B. Kolkovski, and S. Sarov. Structure, alpine evolution and mineralizations of the central rhodopes area (south bulgaria). In *Guide to excursion*

B, ABCD-GEODE Workshop, Borovets, Bulgaria,"St. Kliment Ohridski" University Press, Sofia, 2000.

S. Ji. 85. Ductility of Garnet Indicating High-Temperature Deformation. In *Fault-related Rocks*, pages 280–281. Princeton University Press, 1998. ISBN 978-1-4008-6493-5. doi: 10.1515/9781400864935.280. URL http://www.degruyter.com/document/doi/10.1515/9781400864935.280/html.

T. Kawasaki and Y. Motoyoshi. Ti–in–garnet thermometer for ultrahigh–temperature granulites. *Journal of Mineralogical and Petrological Sciences*, 111(3):226–240, 2016. doi: 10.2465/jmps.150709.

D. S. Keller and J. J. Ague. Crystallographic and textural evidence for precipitation of rutile, ilmenite, corundum, and apatite lamellae from garnet. *American Mineralogist*, 104(7):980–995, July 2019. ISSN 1945-3027. doi: 10.2138/am-2019-6849. URL http://www.degruyter.com/document/doi/10.2138/am-2019-6849/html. Publisher: De Gruyter.

K. Krenn, C. Bauer, A. Proyer, E. Mposkos, and G. Hoinkes. Fluid entrapment and reequilibration during subduction and exhumation: A case study from the high-grade Nestos shear zone, Central Rhodope, Greece. *Lithos*, 104(1-4):33–53, Aug. 2008. ISSN 00244937. doi: 10.1016/j.lithos.2007.11.005. URL https://linkinghub.elsevier.com/retrieve/pii/S002449370700271X.

K. Krenn, C. Bauer, A. Proyer, U. Klötzli, and G. Hoinkes. Tectonometamorphic evolution of the Rhodope orogen. *Tectonics*, 29(4), 2010. ISSN 1944-9194. doi: 10.1029/2009TC002513. URL https://onlinelibrary.wiley.com/doi/abs/10.1029/2009TC002513. _eprint: https://onlinelibrary.wiley.com/doi/pdf/10.1029/2009TC002513.

P. Lessing and R. P. Standish. Zoned Garnet from Grested Butte, Golorado. *American Mineralogist: Journal of Earth and Planetary Materials*, 58(9-10):840–842, 1973.

A. Liati and D. Gebauer. Constraining the prograde and retrograde P-T-t path of Eocene HP rocks by SHRIMP dating of different zircon domains: inferred rates of heating, burial, cooling and exhumation for central Rhodope, northern Greece. *Contributions to Mineralogy and Petrology*, 135(4):340–354, June 1999. ISSN 1432-0967. doi: 10.1007/s004100050516. URL https://doi.org/10.1007/s004100050516.

K. Momma and F. Izumi. VESTA 3 for three-dimensional visualization of crystal, volumetric and morphology data. *Journal of Applied Crystallography*, 44(6):1272–1276, Dec. 2011. ISSN 0021-8898. doi: 10.1107/S0021889811038970. URL https://journals.iucr.org/j/issues/2011/06/00/db5098/. Number: 6 Publisher: International Union of Crystallography.

E. Mposkos and A. Krohe. Petrological and structural evolution of continental high pressure (hp) metamorphic rocks in the alpine rhodope domain (n. greece). In *Proceedings of the 3rd International Conference on the Geology of the Eastern Mediterranean*, volume 221232, 2000.

E. Mposkos, I. Baziotis, and A. Proyer. Metamorphic reprocessing of a serpentinized carbonate-bearing peridotite after detachment from the mantle wedge: A P–T path constrained from textures and phase diagrams in the system CaO–MgO–Al2O3–SiO2–CO2–H2O. *Lithos*, 118(3-4):349–364, Aug. 2010. ISSN 00244937. doi: 10.1016/j.lithos.2010.05.009. URL `https://linkinghub.elsevier.com/retrieve/pii/S002449371000143X`.

E. Mposkos, I. Baziotis, and A. Proyer. Pressure–temperature evolution of eclogites from the kechros complex in the eastern rhodope (ne greece). *International Journal of Earth Sciences*, 101:973–996, 2012.

E. D. Mposkos and D. K. Kostopoulos. Diamond, former coesite and supersilicic garnet in metasedimentary rocks from the Greek Rhodope: a new ultrahigh-pressure metamorphic province established. *Earth and Planetary Science Letters*, 192(4):497–506, Nov. 2001. ISSN 0012821X. doi: 10.1016/S0012-821X(01)00478-2. URL `https://linkinghub.elsevier.com/retrieve/pii/S0012821X01004782`.

F. Nestola, M. Prencipe, P. Nimis, N. Sgreva, S. H. Perritt, I. L. Chinn, and G. Zaffiro. Toward a Robust Elastic Geobarometry of Kyanite Inclusions in Eclogitic Diamonds. *Journal of Geophysical Research: Solid Earth*, 123(8):6411–6423, 2018. ISSN 2169-9356. doi: 10.1029/2018JB016012. URL `https://onlinelibrary.wiley.com/doi/abs/10.1029/2018JB016012`. _eprint: https://onlinelibrary.wiley.com/doi/pdf/10.1029/2018JB016012.

M. Perraki, A. Proyer, E. Mposkos, R. Kaindl, and G. Hoinkes. Raman micro-spectroscopy on diamond, graphite and other carbon polymorphs from the ultrahigh-pressure metamorphic Kimi Complex of the Rhodope Metamorphic Province, NE Greece. *Earth and Planetary Science Letters*, 241(3):672–685, Jan. 2006. ISSN 0012-821X. doi: 10.1016/j.epsl.2005.11.014. URL `https://www.sciencedirect.com/science/article/pii/S0012821X05007703`.

D. J. Prior, J. Wheeler, F. E. Brenker, B. Harte, and M. Matthews. Crystal plasticity of natural garnet: New microstructural evidence. *Geology*, 28(11):1003–1006, 2000.

A. Proyer, G. Habler, R. Abart, R. Wirth, K. Krenn, and G. Hoinkes. TiO2 exsolution from garnet by open-system precipitation: evidence from crystallographic and shape preferred orientation of rutile inclusions. *Contributions to Mineralogy and Petrology*, 166(1):211–234, July 2013. ISSN 0010-7999, 1432-0967. doi: 10.1007/s00410-013-0872-7. URL `http://link.springer.com/10.1007/s00410-013-0872-7`.

A. H. N. Rice and J. I. Mitchell. Porphyroblast textural sector-zoning and matrix displacement. *Mineralogical Magazine*, 55(380):379–396, Sept. 1991. ISSN 0026-461X, 1471-8022. doi: 10.1180/minmag.1991.055.380.08. URL `https://www.cambridge.org/core/product/identifier/S0026461X00056279/type/journal_article`.

A. H. N. Rice, G. Habler, E. Carrupt, G. Cotza, G. Wiesmayr, R. Schuster, H. Sölva, M. Thöni, and F. Koller. Textural Sector-Zoning in Garnet: Theoretical Patterns and

Natural Examples from Alpine Metamorphic Rocks____. *Austrian Journal of Earth Sciences*, 99:70–89, 2006.

C. Schmidt and M. A. Ziemann. In-situ Raman spectroscopy of quartz: A pressure sensor for hydrothermal diamond-anvil cell experiments at elevated temperatures. *American Mineralogist*, 85(11-12):1725–1734, Nov. 2000. ISSN 1945-3027. doi: 10.2138/am-2000-11-1216. URL http://www.degruyter.com/document/doi/10.2138/am-2000-11-1216/html. Publisher: De Gruyter.

B. Stöckhert, H.-J. Massonne, and E. Ursula Nowlan. Low differential stress during high-pressure metamorphism: The microstructural record of a metapelite from the Eclogite Zone, Tauern Window, Eastern Alps. *Lithos*, 41(1):103–118, Aug. 1997. ISSN 0024-4937. doi: 10.1016/S0024-4937(97)82007-5. URL https://www.sciencedirect.com/science/article/pii/S0024493797820075.

Y. Tomioka, Y. Kouketsu, and T. Taguchi. Raman Geobarometry of Quartz Inclusions in Kyanite: Application to Quartz Eclogite from the Gongen Area of the Sanbagawa Belt, Southwest Japan. *The Canadian Mineralogist*, 60(1):121–132, Jan. 2022. ISSN 1499-1276, 0008-4476. doi: 10.3749/canmin.2000097. URL https://pubs.geoscienceworld.org/canmin/article/60/1/121/612053/Raman-Geobarometry-of-Quartz-Inclusions-in-Kyanite.

A. Appendix

A.1. State of thin sections

All provided XA-GO-1E thin sections have "Giessener Format" (48x28mm). The rock sample is embedded in Körapox resin, no thin section is covered. For optical microscopy polish an 1µm monocrystalline diamond bearing compound was run.

thin section	**polish state and use**		**thickness [µm]**
XA-GO-1E_A	diamond	OM	60
XA-GO-1E_B	diamond	OM	50
XA-GO-1E_C	None		60-80
XA-GO-1E_I	diamond	OM	120
XA-GO-1E_II	chemical	EBSD	50
XA-GO-1E_IIIa	diamond	OM	120
XA-GO-1E_IIIb	diamond	OM	140

A.2. EBSD parameter

Hough parameters		**Camera parameters**	
Binning	120-140	Binning	2x2
Theta step size	0.5-1°	Exposure gain	237
Rho Fraction	80-90%	Exposure time	257.77
Max Peak Count	14-20	Snapshot avg.	5
Min Peak Count	3	Background Frames	50
Convolution Mask	9x9, 11x11, (13x13)	Image Processing	1. Background Subtraction
Min Peak Magnitude	1		2. Dynamic Background
Min Peak Distance	9-14		3. Normalize Intensity
Peak Symmetry:	0.5		
Vertical Bias	0-5°		

phase	**point group**	**lattice parameters** [Å]; [°]
garnet (Almandine)_TG1	$[m\bar{3}m]$	11.526
Kyanite_TSL_GH3	[1]	7.124, 7.856, 5.577; 89.990, 101.150, 105.950
Quartz_ETH_keller_DS5	[32]	4.910 5.401
Rutile_TG1	[422]	4.590 2.960

A.3. COR groups: Axial relations and threshold angles

The use of *mTex* to filter large EBSD data sets by the axial relationships between crystallographic orientations of rutile and of garnet derived from Griffiths et al. (2020). COR groups and their axial relations (and angle thresholds for the classification routine) used in this study, ordered according to the routine followed in the *mTex* script, are:

RA:	$< 103 >_{Rt} \| \| \{111\}_{Grt}$	<2°
RC:	$< 001 >_{Rt} \| \| \{110\}_{Grt}$	<5°
RD:	$< 001 >_{Rt} \| \| \{111\}_{Grt}$	<5.5°
RB:	$< 101 >_{Rt} \| \| \{120\}_{Grt}$	<3°
RF:	$< 101 >_{Rt} \| \| \{110\}_{Grt}$	<4°
RE:	$< 100 >_{Rt} \| \| \{111\}_{Grt}$	<5°
RG:	$< 100 >_{Rt} \| \| \{134\}_{Grt}$	<4°
RH:	$< 001 >_{Rt} \| \| \{120\}_{Grt}$	<6°
RJ:	$< 001 >_{Rt} \| \| \{100\}_{Grt}$	<5°

Apart from those axial relationships Hwang et al. (2015) defined specific CORs based on TEM analysis. The crystallographic orientation relationships are defined as:

COR1:	$< 103 >_{Rt}$	$\| \| \{111\}_{Grt}$	COR4:	$< 001 >_{Rt}$	$\| \| \{111\}_{Grt}$
	$< 100 >_{Rt}$	$\| \| \{110\}_{Grt}$		$< 100 >_{Rt}$	$\| \| \{112\}_{Grt}$
	$< 103 >_{Rt}$	$\| \| \{100\}_{Grt}$		$< 100 >_{Rt}$	$\| \| \{110\}_{Grt}$
COR2:	$< 103 >_{Rt}$	$\| \| \{111\}_{Grt}$	COR4b:	$< 001 >_{Rt}$	$\| \| \{111\}_{Grt}$
	$[0\bar{1}0]_{Rt}$	$\| \| (4\bar{3}\bar{1})_{Grt}$		$< 110 >_{Rt}$	$\| \| \{112\}_{Grt}$
	$< 110 >_{Rt}$	$\| \| \{111\}_{Grt}$		$< 110 >_{Rt}$	$\| \| \{110\}_{Grt}$
COR2':	$< 103 >_{Rt}$	$\| \| \{111\}_{Grt}$	COR5:	$< 001 >_{Rt}$	$\| \| \{100\}_{Grt}$
	$[010]_{Rt}$	$\| \| [4\bar{3}\bar{1}]_{Grt}$		$< 110 >_{Rt}$	$\| \| \{100\}_{Grt}$
COR3:	$< 103 >_{Rt}$	$\| \| \{111\}_{Grt}$	COR5b:	$< 001 >_{Rt}$	$\| \| \{100\}_{Grt}$
	$< 100 >_{Rt}$	$\| \| \{112\}_{Grt}$		$< 100 >_{Rt}$	$\| \| \{100\}_{Grt}$
	$< 120 >_{Rt}$	$\sim \{134\}_{Grt}$			

A.4. mTex: COR classification (Version Rt_CORcat_28_01_2021_5pt4pt0)

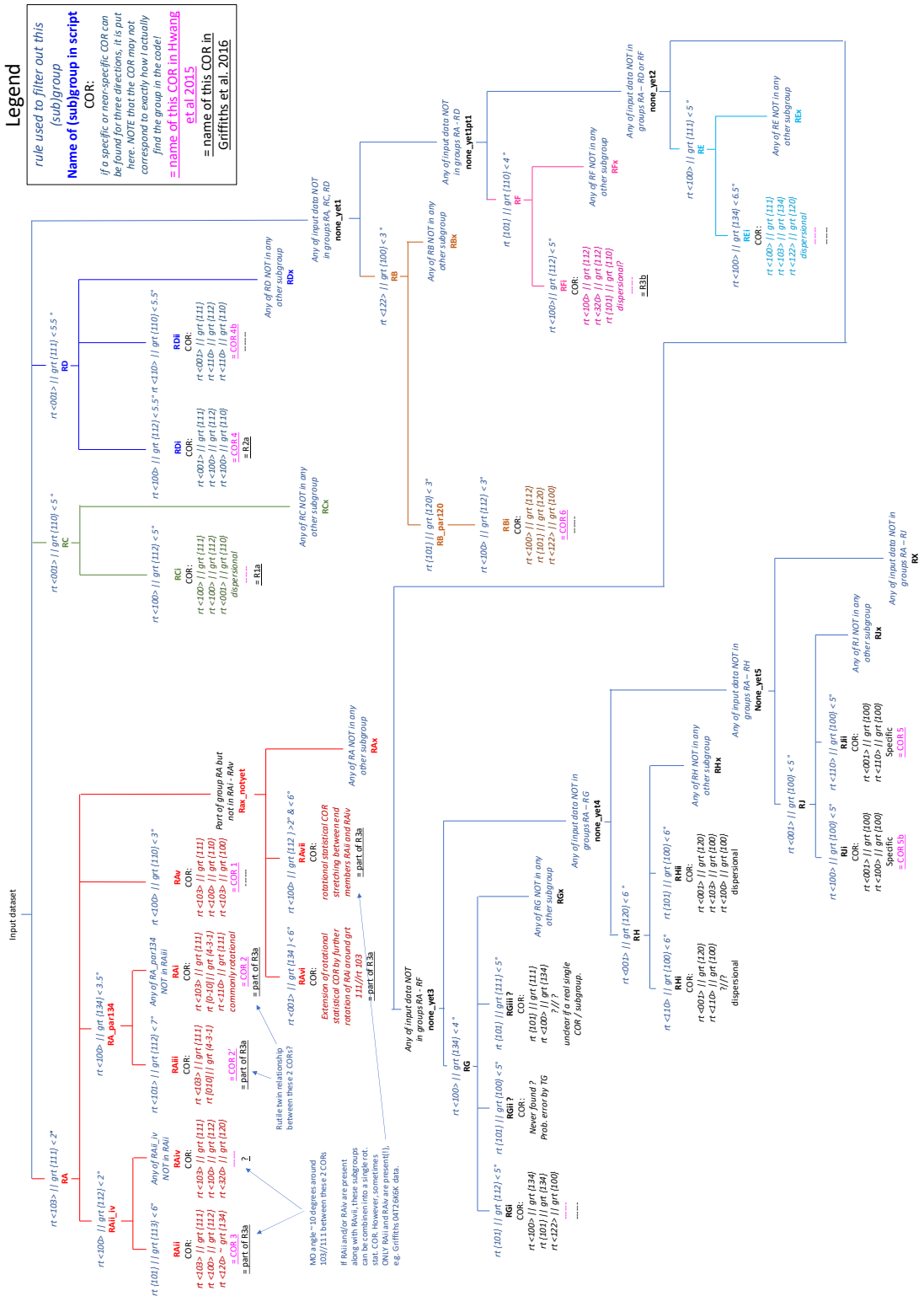

A.5. COR classification results

Table A.1.: All measured rutiles (all domains, all types, all SPOs)

Axial relationship groups			Specific CORs		
n(total)		success	n(total)		success
518		90.3%	422		81.5%
	n	distr.		n	distr.
RA	334	71.4%	RAi	180	53.9%
			RAii	46	13.8%
			RAiii	53	15.9%
			RAiv	7	2.1%
			RAv	4	1.2%
			RAvi	37	11.1%
			RAvii	2	0.6%
			RAx	5	1.5%
RB	33	7.1%	RBi	26	78.8%
			RBx	7	21.2%
RC	23	4.9%	RCi	14	60.9%
			RCx	9	39.1%
RD	5	1.1%	RDi	5	100.0%
RE	5	1.1%	REi	4	80.0%
			REx	1	20.0%
RF	4	0.9%	RFi	3	75.0%
			RFx	1	25.0%
RG	47	10.0%	RGi	3	6.4%
			RGiii	36	76.6%
RH	17	3.6%	RHi	1	5.9%
			RHii	1	5.9%
			RHx	15	88.2%

Table A.2.: Trail rutile inclusions (trail domain, equant, no SPO)

Axial relationship groups			Specific CORs		
n(total)		success	n(total)		success
178		83.1%	115		64.6%
	n	distr.		n	distr.
RA	67	45.3%	RAi	28	41.8%
			RAii	21	31.3%
			RAiii	13	19.4%
			RAiv		0.0%
			RAv	1	1.5%
			RAvi	3	4.5%
			RAvii		0.0%
			RAx	1	1.5%
RB	19	12.8%	RBi	15	78.9%
			RBx	4	21.1%
RC	19	12.8%	RCi	11	57.9%
			RCx	8	42.1%
RD	0	0.0%	RDi	0	0.0%
RE	4	2.7%	REi	3	75.0%
			REx	1	25.0%
RF	2	1.4%	RFi	1	50.0%
			RFx	1	50.0%
RG	22	14.9%	RGi	1	4.5%
			RGiii	17	77.3%
RH	15	10.1%	RHi	1	6.7%
			RHii	0	0.0%
			RHx	14	93.3%

Table A.3.: Needle rutile inclusions (needle domain, needle rutile with SPO)

Axial relationship groups			Specific CORs		
n(total)		success	n(total)		success
227		98.2%	216		95.2%
	n	distr.		n	distr.
RA	207	92.8%	RAi	124	59.9%
			RAii	22	10.6%
			RAiii	25	12.1%
			RAiv	5	2.4%
			RAv	3	1.4%
			RAvi	22	10.6%
			RAvii	1	0.5%
			RAx	4	1.9%
RB	7	3.1%	RBi	5	71.4%
			RBx	2	28.6%
RC	1	0.4%	RCi	1	1.0%
			RCx	0	0.0%
RD	3	1.3%	RDi	3	1.0%
RE	0	0.0%	REi	0	0.0%
			REx	0	0.0%
RF	1	0.4%	RFi	1	1.0%
			RFx	0	0.0%
RG	4	1.8%	RGi	0	0.0%
			RGiii	4	100.0%
RH	0	0.0%	RHi	0	0.0%
			RHii	0	0.0%
			RHx	0	0.0%